



**HAL**  
open science

## Shale tectonic processes : Field evidence from the Parras Basin (north-eastern Mexico)

Eric Deville, Clement Dutrannoy, Julien Schmitz, Benoit Vincent, Eric Kohler, Abdeltif Lahfid

### ► To cite this version:

Eric Deville, Clement Dutrannoy, Julien Schmitz, Benoit Vincent, Eric Kohler, et al.. Shale tectonic processes : Field evidence from the Parras Basin (north-eastern Mexico). *Marine and Petroleum Geology*, 2020, 122, pp.104688. 10.1016/j.marpetgeo.2020.104688 . hal-03118704

**HAL Id: hal-03118704**

**<https://ifp.hal.science/hal-03118704>**

Submitted on 21 Sep 2022

**HAL** is a multi-disciplinary open access archive for the deposit and dissemination of scientific research documents, whether they are published or not. The documents may come from teaching and research institutions in France or abroad, or from public or private research centers.

L'archive ouverte pluridisciplinaire **HAL**, est destinée au dépôt et à la diffusion de documents scientifiques de niveau recherche, publiés ou non, émanant des établissements d'enseignement et de recherche français ou étrangers, des laboratoires publics ou privés.



Distributed under a Creative Commons Attribution - NonCommercial 4.0 International License

# 1 **Shale tectonic processes: Field evidence from the Parras Basin (North-** 2 **Eastern Mexico)**

3

4 Eric Deville<sup>1\*</sup>, Clement Dutrannoy<sup>1-2</sup>, Julien Schmitz<sup>1</sup>, Benoit Vincent<sup>1-3</sup>, Eric Kohler<sup>1</sup>,  
5 Abdeltif Lahfid<sup>1-4</sup>

6

7 <sup>1</sup> IFPEN, 1-4, av. de Bois Préau, 92 852 Rueil-Malmaison, France

8 <sup>2</sup> Present address: Veolia, 28 bd de Pesaro, 92000 Nanterre, France

9 <sup>3</sup> Present address: Cambridge Carbonate limited, 707 Warwick Rd, Solihull B91 3DA, UK

10 <sup>4</sup> Present address: BRGM, 3 av. Claude Guillemin BP 36009, 45060 Orléans Cedex, France

11

## 12 **ABSTRACT**

13

14 Major décollements located within buried overpressured shale commonly develop in thrust fronts,  
15 accretionary prisms and sedimentary deltas controlled by gravity tectonics. In seismic data, it is  
16 possible to observe only large scale deformation of what is commonly designed as mobile shale but  
17 the precise geometry and the dynamic evolution of these bodies remains poorly understood. It is often  
18 difficult to define if we are dealing with ductile or brittle deformation and to understand the role of the  
19 fluids in time and space during deformation. For this reason, large scale outcrops were studied in the  
20 Parras Basin (Mexico), which makes possible a direct observation of the shale tectonic processes. This  
21 work suggests changes in space and time of the deformation processes which occurred within the shale  
22 formation hosting the decollement. Distributed deformation was observed within the shale formation  
23 hosting the decollement compared to more localized deformation above. Also a change of the rheology  
24 of the shale over time occurred progressively toward brittle processes in the whole sedimentary pile.  
25 XRD and microscopic studies have shown that diagenetic processes are favored in the shear zones of  
26 penetrative deformation leading notably to reverse gradient of illitization. The isotopic analysis of  
27 cements in veins and the study of associated fluid inclusions have shown that fluid dynamics also  
28 evolved during time showing notably evidence for widespread fluid migration issued from rocks  
29 located below the decollement during the beginning of the deformation. Progressively, the tectonic  
30 system located above the decollement tends to be preserved from fluid migration coming from below  
31 the decollement and to be influenced only by local fluid migration (closed system).

32

33 **Key words:** shale tectonics, mobile shale, decollement, deformation, fluids, diagenesis

34 \* Corresponding author E-mail address: [eric.deville@ifpen.fr](mailto:eric.deville@ifpen.fr)

35

36 **Highlights:**

37

38 ➤ Outcrops were studied in NE Mexico to understand better the processes of shale  
39 tectonics

40

41 ➤ Shale rocks deformation evolved from ductile toward brittle processes

42

43 ➤ Fluid migrations occurred from below the decollement during early deformation

44

45 ➤ The thrust wedge evolved progressively toward a closed hydrodynamic system

46

47  
48  
49  
50  
51  
52  
53  
54  
55  
56  
57  
58  
59  
60  
61  
62  
63  
64  
65  
66  
67  
68  
69  
70  
71  
72  
73  
74  
75  
76  
77  
78  
79

## **1. Introduction**

In most of the tectonic fronts of convergent orogens (including accretionary prisms, fold and thrust systems in mountain belts) but also in thick deltaic systems controlled by gravity tectonics on passive margins, except when evaporates are present, decollement processes occur commonly in overpressured shale. During shale tectonics associated with this type of decollement, shale is deformed in the deepest parts close to the decollement generating poorly understood structures which are commonly named by a number of generic terms (such as mobile shale, shale diapirs, clay diapirs, mud diapirs, argillokinetic structures, etc.; Bruce, 1973; Brown, 1990; Bradshaw and Watkins, 1994; Cohen and McClay, 1996; Huh et al., 1996; Morley and Guerin, 1996; Morley, 2003; Van Rensbergen and Morley, 2000, 2003; Van Rensbergen et al., 2000, 2003a and b; Corredor et al., 2005; Briggs et al., 2006; Deville et al., 2006, 2010; Wiener et al., 2010; Elsley and Tieman, 2010). These terms are currently used to describe geometric features on the seismic data but with only geophysical data and without direct constraints provided by wells or field observations, it is difficult to define exactly what are the prevailing deformations processes which occur within these shale-rich bodies (see an example in 1). These volumes of sediments poorly imaged in seismic data are commonly considered as mobile shale bodies but generally, authors do not prejudge about the nature, the structure and the genetic processes at the origin of the deformation of these shale-rich bodies. Present-day understanding of subsurface clay-rich sediment deformation remains relatively low and commonly made by comparison with the larger literature on salt tectonics (Morley and Guerin, 1996). However, these processes clearly differ from salt mobilization, notably by the crucial role taken by the fluid dynamics that is able to induce sediment liquefaction and controls overpressured shale deformation. In most cases, on seismic lines, it is difficult to define if sediment deformation occurred as a brittle or a ductile process, even though this implies drastic differences in the rheology of the material involved and the modes of deformation (see discussion in Wood, 2010, 2012). When interpreting seismic data, what is usually designated as mobile shale corresponds to volumes of rocks whose global geometry suggests a ductile deformation (pillow shapes, deformed cores of large anticlines suggesting diapiric shapes). It is generally difficult to define if this deformation occurred as liquefaction of sediments, or as flow of ductile but still stratified material or else as deformation of intensively fractured rocks at depth (Deville et al., 2003; 2006; 2010). With the improvement

80 of seismic data, it progressively appeared that what was considered as shale diapir is much  
81 more restricted than previously thought (Van Rensbergen et al., 2003).  
82 The widespread occurrence of shale tectonic processes, their common association with  
83 hydrocarbon producing areas and their influence on the development of a wide range of  
84 sedimentary basins require new studies of these phenomena. For a better understanding of the  
85 deformation processes of what is commonly named mobile shale, we made field studies on an  
86 outcropping case. The objective of this work was to study outcrops associated with a major  
87 decollement zone in shale located at the base of a thick tectonic wedge. In active or recent  
88 thrust systems developed on top of a decollement in shale or on top of intensively deformed  
89 shale, because of the burial, it is usually impossible to study the shale deformation directly on  
90 wide surface outcrops. For this reason, we choose a case study in the Parras Basin in northern  
91 Mexico (Fig. 2), which corresponds to an area where exposures of a large decollement system  
92 can be studied thanks to a late uplift and erosion (Figs. 3, 4). The objective of this study was  
93 to better understand the deformation mechanisms of the so-called mobile shale notably close  
94 to the decollement level and in the cores of clay-rich anticlines, as well as the scale factors  
95 (microstructures *vs.* macrostructures). We also wanted to use this outcropping analog to better  
96 understand the interactions between deformation - migration of fluids - diagenesis in tectonic  
97 fronts characterized by decollement in shale.

98

## 99 **2. Geological framework**

100

### 101 *2.1. Depositional setting*

102

103 What is commonly named the 'Parras Basin' is a part of the Mexican Laramide tectonic front  
104 which includes the deltaic uppermost Cretaceous and Early Tertiary terms forming the detrital  
105 stratigraphic series of the Jurassic-Cretaceous of the Sierra Madre Oriental in the area of  
106 Parras and Saltillo (Figs. 2, 3). The Parras Basin develops south of the Popa and Sabinas  
107 basins and it is limited to the northwest by the Coahuila platform and to the south by the front  
108 of the Sierra Madre Oriental (Weidie et al., 1966, 1978; Weidie and Murray, 1967; McBride  
109 et al., 1971, 1973, 1974, 1975; Tardy et al., 1975; Tardy, 1980; Soegaard et al., 2003) (Fig. 2,  
110 3). The area studied in the Parras basin shows wide outcrops partly hampered by the  
111 development of recent alluvial systems. The cores of the anticlines and the lower part of the  
112 series, which includes highly deformed shale, outcrop in good conditions on several hundred  
113 of km<sup>2</sup> (Fig. 4). The oldest rocks present in the study area which form the stratigraphic base of

114 the Parras basin correspond to the Cretaceous carbonate of the Coahuila group (Lehmann et  
115 al., 1999; Lawton et al., 2001). The sedimentary base of the Parras basin consists of  
116 Campanian marine shale (Parras shale formation; McBride et al., 1974; Bartolini et al., 1995,  
117 2001; Ifrim et al., 2015). Above, the sediments of the Parras Basin correspond to a deltaic  
118 system (Difunta group; Murray et al., 1959; 1960; 1962) essentially of Maastrichtian age and  
119 for a minor part of Paleocene age (Fig. 5). The Difunta Group corresponds to a succession of  
120 stratigraphic cycles (Warning and McBride, 1976; Wollenben, 1977; Soegaard et al., 2003;  
121 Fig. 5). The various formations correspond to different sedimentation areas sourced by clastic  
122 inputs, from the upstream deposits of a flood plain to a downstream turbidite system. This  
123 paleo-delta was sourced by the erosional products of the Sierra Madre structured during the  
124 Laramide period. During Campanian-Maastrichtian times, the Parras Basin was located at the  
125 connection between the Western Interior Seaway of the North American continent and the  
126 Gulf of Mexico (Robinson-Roberts and Kirschbaum, 1995). At that time, this area was part of  
127 a large continental shelf open towards the Gulf of Mexico to the east and bordered to the west  
128 by the arc of the Sierra Madre. The thick accumulation of the sediments of the Difunta Group,  
129 up to 6000 m (McBride et al., 1975), was probably related to a flexural basin installed on a  
130 thinned continental crust which corresponded to the western margin of the Gulf of Mexico.  
131 The common absence of fragments of carbonates in the sandstone Difunta Group shows that  
132 the carbonated reliefs of the Sierra Madre Oriental were not the source of the clastic input in  
133 the Parras Basin. The delta was most probably fed by a fluvial system which brought the  
134 material from the magmatic rocks of the Sierra Madre Occidental (Guerrero arch) to the west.  
135 Deltaic series are composed of fine to very-fine-grained sandstone with some exceptional  
136 layers of medium-grained sandstone. Periods of eustatic drop result in forced regressions  
137 whose deposits (shoreface and fluvial deposits of the Las Imagenes and Las Encinas  
138 formations) correlate across the basin for tens of kilometers (Soegaard et al., 2003). On top of  
139 the Parras shale, a first progradation of the delta shows that the Upper Campanian clastic  
140 input issued from the erosion of the reliefs of the Sierra Madre were initially too high in  
141 volume compared to the available space. This prograding series is designated as the Cerro del  
142 Pueblo formation in the literature and it is late Campanian in age (McBride, 1974; Eberth et  
143 al., 2004; Vega et al., 2018). The transition Campanian-Maastrichtian is located at the top of  
144 the Cerro del Pueblo which is consistent with the data published by McBride et al. (1974) and  
145 Vega et al. (2018). Above the shoreface of the top of the Cerro del Pueblo formation, beach  
146 deposits are capped with red fluviolacustrine continental series deposited in a delta plain (up  
147 to almost 1000 m thick). This unit is mentioned as the Cerro Huerta formation in McBride et

148 al. (1974; 1975). On top of the Cerro Huerta formation, a gradual transgression led to the  
149 deposition of marine shoreface series. This frankly marine episode is designated as the Cañon  
150 del Tulle formation (McBride, 1974). The maximum flooding surface of this transgression is  
151 situated in deep marine clays-rich layers. Thin turbidite systems developed during the  
152 following period of high sea level, probably sourced by hyperpycnal flows generated by  
153 seasonal flooding of rivers upstream. On top of these turbidite systems, a new regression is  
154 correlated with an important eustatic fall (about 50 m) during Upper Cretaceous. This forced  
155 regression caused the deposit of sandy shoreface systems directly on top of deeper marine  
156 deposits. This corresponds to the Las Imagenes formation, which includes sandbars tens of  
157 kilometers long.

158 Then, a new transgression (Cerro Grande formation) was associated with more marine  
159 deposits (shallow marine clays) punctuated by several minor episodes of regression  
160 (prograding shoreface). On top of these marine deposits, a new forced regression (Las Encinas  
161 formation) induced shoreface and then red fluvial sandstones deposition which form a strong  
162 and distinctive bar. It marks the transition to the Paleocene (McBride et al., 1974; Diaz et al.,  
163 2017; Vogt et al., 2016; Martinez-Diaz et al., 2017; Vega et al., 2018). Higher up in the series,  
164 a last transgression was responsible for the deposition of deep marine deposits (Rancho  
165 Nuevo/ Potrerillos formation) which consist of marine shale punctuated by gravity flow  
166 deposits that form tabular zones at the top of the series of the Parras basin.

167

## 168 *2.2. Tectonic framework*

169

170 The study area corresponds to the Laramide front that was mostly active during Early Tertiary  
171 times (McBride et al., 1974). At that time, the compressive front of the Sierra Madre Oriental  
172 extended on the western margin of the Gulf of Mexico. During the Neogene, the entire  
173 western edge of the Gulf was uplifted (especially along the arch of Tamaulipas), which led to  
174 erosion responsible for the outcrop of the former compressive structures (McBride et al.,  
175 1974; Gray et al., 2001). The Eastern Parras Basin is preserved in a large syncline trough  
176 showing a north-south axis (Fig. 3), the edges of this trough being largely eroded (especially  
177 the western edge situated beside the Coahuila arch; Fig. 3, 4). Therefore, it is possible to study  
178 directly wide outcrops corresponding to a complete geological section of the Parras basin  
179 resulting of the Laramide compression (Fig. 4). As it has been originally proposed by Tardy et  
180 al. (1975), a generalized decollement occurred within the Parras marine shale. Indeed, the  
181 deltaic system of the Parras Basin was affected by intense deformation including decollement

182 tectonics in Campanian marine shale (Parras shale formation). In the area, the Early  
183 Cretaceous sediments are only involved in long wave-length folding (Coahuila block),  
184 whereas the Upper Cretaceous-Paleocene is deformed in a system of folds and thrusts (see  
185 especially the mapping made by McBride et al., 1974, 1975, Tardy et al., 1975 and Tardy,  
186 1980). Along section of Fig. 3B, the shortening is estimated to be higher than 10 km. The  
187 deformation related to decollement tectonics occurred in marine open environment and the  
188 related structures were progressively covered by marine sediments towards the tectonic front  
189 (marine clays and turbidite deposits gravity and mass flows, *e.g.* Paleogene Rancho Nuevo or  
190 Potrerillos formation; Fig. 4). The age of the decollement is then known thanks to the  
191 presence of these growth layers of Paleocene age covering the tectonic front (Lawton et al.,  
192 2001). Indeed, the latest layers preserved in the Parras Basin correspond to siliciclastic  
193 deposits dated of Paleocene age, *e.g.* Potrerillos formation of the Mac Bride et al. (1974) or  
194 Rancho Nuevo of Soegaard et al. (2003). This formation shows fan geometries which are  
195 compatible with syntectonic sedimentation. As a consequence, the deposition of this  
196 formation can be considered as coeval to the observed deformation in the Parras Basin (Late  
197 Maastrichtian-Paleocene deformation).

198

### 199 **3. Material and methods**

200

201 A sequence of different approaches has been used to characterize deformation, fluid migration  
202 and diagenesis: field structural geology, optical microscopy of veins, XRD of clays, study  
203 fluid of inclusions in calcite and quartz, stable isotope composition of carbonate cements,  
204 study of organic matter maturity (using Rock-Eval and Raman techniques) and thermal  
205 modeling. The objective of this work was to better understand the evolution of the  
206 deformation processes, their physical conditions, and to identify the nature and origin of the  
207 fluids associated with this deformation. Large scale field mapping supported with Landsat and  
208 Spot satellite imagery was made NW of Saltillo (Figs. 6, 7). This field study included also  
209 microstructural observations and measurements.

210 Veins have been studied by optical microscopy including catholuminescence. Petrographic  
211 investigation includes optical microscopy performed on half-stained thin sections (Alizarin  
212 red S + potassium ferricyanide; Lindholm and Finkelman, 1972), and cathodoluminescence  
213 (CL; Machel, 2000).

214 After extraction of the fine fraction, with a particle size of less than 2  $\mu\text{m}$ , the X-ray  
215 measurements were carried out on oriented preparations which are air dried or saturated with



216 ethylene glycol. Saturation with K or Mg followed by ethylene glycol (EG) solvation is a  
217 classical method used to identify high-charge smectite. XRD patterns were acquired using Cu  
218 radiation with  $0.017^\circ 2\theta$  step size and  $91\text{s}\cdot 2\theta^{-1}$  counting time with a position-sensitive detector  
219 on an X'pertPro Panalytical diffractometer. For the identification of minerals in a rock and  
220 clays characterization, X-ray profiles are acquired in Bragg-Brentano geometry. The  
221 identification of minerals is achieved using the crystal-chemical database from the  
222 Mineralogical Society of America and the Crystallography Open Database (COD).

223 A thermobarometric reconstruction of the diagenetic history was carried out by the study of  
224 fluid inclusions in the different generations of cements filling veins (including calcite and  
225 quartz) to define the composition and temperature-pressure conditions of the fluid having  
226 circulated in the Parras Basin since the end of the Cretaceous. This study attended to  
227 characterize the physical conditions of the different fluids that participated in the  
228 mineralization of diagenetic phases and to better understand the interactions between  
229 deformation processes, fluid migration and diagenesis (Roedder, 1984; Shepherd et al., 1985;  
230 Goldstein, 2001). Microthermometry measurements were made with a Nikon eclipse LV100  
231 optical microscope using a video system connected to a computer coupled to a Linkam  
232 turntable THMSG 60. Cooling was ensured by a circulation of liquid nitrogen. Calibration  
233 was made at  $-56.6^\circ\text{C}$  with a quartz sample of Calanda containing inclusions of pure  $\text{CO}_2$ .

234 Isotopic analyses of carbonate cements in mineralized veins were performed on cements from  
235 fractures localized in the carbonates of the Coahuila Group and above these carbonates, in the  
236 Parras shale formation, below, within, and above the decollement zone. Carbonate powders  
237 were sampled with a microdrill under a binocular from the calcite spars and the cataclasites.  
238 They were reacted with 100% phosphoric acid (density  $>1.9$ , Wachter and Hayes, 1985) at  
239  $75^\circ\text{C}$  using a Kiel III online carbonate preparation line connected to a ThermoFinnigan 252  
240 massspectrometer. All values are reported in per mil relative to V-PDB by assigning a  $\delta^{13}\text{C}$   
241 value of  $+1.95\text{‰}$  and a  $\delta^{18}\text{O}$  value of  $-2.20\text{‰}$  to NBS19. Reproducibility was checked by  
242 replicate analysis of laboratory standards and is better than  $\pm 0.02$  ( $1\sigma$ ).

243 73 Rock-Eval<sub>6</sub> analyses (Lafargue et al., 1998) were made in the study area and among them  
244 58 were made on samples from the Parras shale formation (where the decollement is located)  
245 and the others on samples from the formations which are stratigraphically located above the  
246 Parras shale formation (see supplementary material; table SII).

247 Paleothermometry by Raman Spectroscopy of Carbonaceous Material (RSCM) was applied  
248 on four selected samples located in the decollement zone and just above (samples 8B, 11,  
249 120C, 113C; Fig. 6A). RSCM is a method based on the structuration degree of the residual

250 organic matter to estimate the thermal peak undergone by rock samples. This method was  
251 initially developed in the range 300-700°C by Beyssac et al. (2002). The method has been  
252 then expanded to be used for lower thermal conditions in the range 150-300°C (Lahfid et al.,  
253 2010). RSCM method allowed completing Rock-Eval results for high maturity values.  
254 Temperatures defined by microthermometry and Raman spectroscopy were finally used to  
255 reconstruct the burial history of the Parras Basin by 1D modeling performed with the  
256 GENEX-GENTECT software®. The location of the 1D model has been chosen at the place  
257 where samples 64A and 68A were collected (Fig. 6B). The data used for the modeling include  
258 lithostratigraphic descriptions of each formation, their thickness and the estimated erosion as  
259 summarized in Fig. 6B. Thermal parameters of these formations were chosen taking into  
260 account their lithology from the default data base of the GENEX software.

261

## 262 **4. Results**

263

### 264 *4.1. Deformation processes in and around the decollement zone*

265

266 The Cretaceous carbonate formations of the Coahuila arch which are located below the  
267 decollement zone are affected by long wave-length folding processes contrary to the  
268 formations located above the decollement (Figs. 3, 4, 6, 7). In the area studied, they are  
269 simply tilted towards the east or south-east (Figs. 3, 4, 6, 7). They are simply tilted towards  
270 the east or south-east. They show evidence of intense fracturing associated with well-  
271 developed calcite cements (Fig. 8). Outcrops of Cretaceous Parras shale located below the  
272 basal decollement show a well-preserved continuous stratification and abundant fractures  
273 perpendicular to the stratification and dispersed in direction (Fig. 8). Dips of the beds of the  
274 lower Parras shale show a conform bedding to those of the carbonates of the Coahuila arch  
275 (tabular levels tilted towards the east and south-east due to the Coahuila arch doming). The  
276 decollement level is located at the base of the Parras formation in the southern part (inner  
277 zone), while it is located higher in the stratigraphic series close (less than a hundred meters) to  
278 the lower sandstone formation (C. del Pueblo) north of the study area (outer zone toward the  
279 tectonic front). The outcrops observed in the basal decollement zone are characterized by  
280 several meters of intensely sheared rocks, cataclastic carbonate rocks and tectonic breccias  
281 (Fig. 9). In many places, diagenetic concretions are observed in the form of centimetric to  
282 decimetric rounded calcium carbonate concretions and tubes corresponding probably to  
283 former fluid circulation conduits in the fracture system (Fig. 9). Rocks located above the

284 decollement show evidence for former percolation of fluids, which are characterized either in  
285 a very diffuse way in the argillaceous rocks, or more focused in shear planes or in the form of  
286 fluid chimneys (Fig. 10). Gradually, above the basal decollement, intensely deformed clay-  
287 rich areas are encountered showing a scaly fabric where the initial stratification is no longer  
288 visible. The initial stratification can only be recognized from the alignment of boudinated  
289 layers of sandstones preserved in clay-rich masses (Figs. 10, 11; Figs. S2). Obviously, the  
290 clay-rich levels were affected by strong creeping, while the sandstone beds ruptured in  
291 different strands. These structures are clear evidence of a period of ductile deformation of  
292 shale rocks. Subsequently to the ductile deformation, shale rocks were intersected by fault  
293 planes associated with calcite cements (Fig 12).

294

295 *The shale-rich core of the main folds.* In the study area, several structural zones can be  
296 distinguished (Fig. 3, 4): (1) an outer area of relatively tight frontal folds related to an  
297 imbricated stack of thrust sheets, (2) an area transported with relatively little deformation only  
298 marked by reverse faults with moderate throws, and (3) an inner large wavelength folds area.  
299 As mentioned above, the main basal decollement level located in the Parras shale propagated  
300 up in the stratigraphic series toward the north. Consequently, there are large volumes of  
301 Parras shale which are deformed in the core of the folds the southern part of the study area  
302 (more than five hundred meters thick). The cores of the main folds do not show thick  
303 continuous sandstone beds. The center of the main folds of the studied area consists mainly of  
304 scaly-fabric shale where the initial stratification can only be recognized very punctually from  
305 the boudinage of few recognizable sandstone beds (Figs. 10, 11; Figs. S2, S3 in  
306 supplementary material). In most cases, even sandstones failed to inform us directly about the  
307 initial stratification as they correspond to isolated boudinated elements in shale-rich masses  
308 (Figs. 10, 11; Fig. S3). Only traces corresponding to shale welds between the boudins are  
309 visible within the shale rocks (Fig. 10; Fig. S3). Also, in many places, we observed probable  
310 former conduits of fluid flows in the form of concretion tubes of several of centimeter of  
311 diameter with a complex geometry, generally made of sandy-argillaceous rocks cemented by  
312 carbonates (Figs. 10, 11). Very characteristically, the core of the main folds of the study area  
313 was the place of an intense penetrative deformation in the early stages of folding. In contrast,  
314 during the progressive evolution of the deformation, the cores of the folds were affected by  
315 brittle processes associated with striated calcite precipitation in the fault planes (Fig. 12).  
316 Therefore, the cores of these main folds were the place of a rheological change characterized  
317 by an evolution from intensively penetrative deformation to localized brittle deformation.

318 Contrary to the core of the folds, stratifications are well-preserved In the post-Parras shale  
319 formations where thick sandstone beds are continuous and only little deformed (Figs. 13, 14).  
320 The transition between the scaly shale and the continuous sandstone beds is sharp (few  
321 meters) and it is probably mainly controlled by the initial lithology before deformation, the  
322 penetrative deformation being principally localized in areas with little sandstone levels. In the  
323 upper part of the marine Parras shale formation stratifications are perfectly preserved and the  
324 dips are consistent with those of the overlying formations (especially with the formation Cerro  
325 del Pueblo).

326

327 *Fracture systems.* Above the basal decollement, numerous low dipping faults corresponding  
328 to localized mineralized shear bands (several centimeters to several tens of centimeters thick)  
329 developed in the lower part of the thrust wedge (Fig. 15). These planes show slickensides  
330 made of calcite (Fig. 16). These faults are either parallel to the bedding (flat areas), or slightly  
331 oblique to the stratification (ramp areas). In some places, transitions from flat to ramp can be  
332 observed (Fig. 15). The slickenlines have a well-regulated average strike of N15° (Fig. 16).  
333 This direction is interpreted as the main transport direction during the main deformation phase  
334 (north verging). Frequently, the striated calcite planes are affected by open subvertical  
335 fractures, roughly perpendicular to the direction of displacement (Fig. 16). In many cases, we  
336 observe recurring figures showing that flat shears with calcite crystallization are located a few  
337 centimeters just above sandstone beds (Fig. 15).

338 Many cataclasites layers are connected with the low angle fault planes. Either they occupy  
339 part of the fault plane (in this case the fault zone includes a well-preserved crystalline calcite  
340 part and a cataclasite part) or they appear in the fault planes as pillows that can form locally  
341 several meters thick lenses (Fig. 17). These pillows are interpreted as mobilization of the  
342 cataclastic material as injectites which has been displaced in the fault plane and locally  
343 accumulated in lenses. The cataclastic material is made of mechanically crushed calcite partly  
344 re-cemented by calcium carbonate cements. These lenses of cataclasites contain frequently  
345 polygenic breccia elements issued from the surrounding rocks forming real tectonic breccias  
346 (Fig. 17). In different places, we observed sedimentary sandstone dikes. Some of them are  
347 tightly folded in a way that reflects a flattening perpendicular to the horizontal plane. We  
348 interpret the setting of these dikes as occurring in an early stage, at least prior to the main  
349 compaction of the surrounding clays-rich sediments (Fig. S1 in supplementary material). The  
350 study of fractures which are related to the main tectonic event has shown that the calcite-  
351 cemented fractures have clear orientation changes between areas in the decollement zone and

352 the fracture system observed above the decollement zone. In the lower part of the thrust  
353 wedge which is essentially made of shale-rich sediments associated with small sandstone  
354 beds, the subvertical fracture have an average orientation perpendicular to the direction of  
355 transport observed on the low angle fault planes (Fig. 14). In the few thin sandstone beds (<  
356 10 cm thick), however, fracture networks are generally conjugated with an angle of about 40°  
357 with respect to the direction N15°. Fractures located in the upper part of the thrust wedge are  
358 dominantly subvertical with the same direction as the slickenlines along the fault planes  
359 (roughly N15°) which is interpreted as the direction of shortening (Fig 14). These subvertical  
360 fractures are filled with calcite on top of the Parras shale formation and the Cerro del Pueblo  
361 formation. However, above the clay-rich layers of the Cerro Huertas formation, these  
362 fractures are still well-expressed with the same dominant orientation N15° but they are no  
363 longer filled with thick calcite cements.

364

#### 365 *4.2. Syn-kinematic diagenesis*

366

367 *Veins.* The study by optical microscopy and CL has shown several generations of syn-  
368 kinematic diagenetic veins. The following sequence of mineral precipitation was  
369 distinguished (Fig. 18): 1) *Calcite.* Large early veins filled with calcite cements have been  
370 observed in the Cretaceous carbonates of the Coahuila group, as well as in the different  
371 structural levels distinguished in the Parras shale formation (Fig. 19). In the Coahuila group,  
372 these veins correspond to an early generation of large calcite crystals very commonly twinned  
373 and often distorted and showing a faint sector zoning under CL, despite an overall dull brown  
374 homogeneous luminescence. The host rock appears intensively affected by open fractures,  
375 with a rather isotropic distribution. These large calcite veins are also present in the  
376 decollement zone and above. Some calcite bands locally exceed 50 cm of thickness. These  
377 veins are also well-developed at the top of the Parras shale formation and the Cerro del  
378 Pueblo formation where they are made up mainly of large subvertical open fractures oriented  
379 mainly N15° (see above). We did not observe such massive veins above the Cerro Huertas  
380 formation. 2) *Cataclasites.* The calcite veins have been deformed (minerals are often folded),  
381 sheared (shear bands within calcite cements) and, in many cases, the calcite cements have  
382 been crushed generating cataclasites (Fig. 20). These cataclasites bodies locally include  
383 brecciated polygenic elements from the surrounding rocks from macroscopic to microscopic  
384 scale. 3) *Quartz.* Subsequent to the development of cataclasites, mostly quartz precipitation  
385 occurred. Quartz is expressed either by large euhedral crystals, or as microcrystalline veins.

386 Quartz veins were either newly formed or they re-used the former calcite veins (Fig. 21). In  
387 the latter case, the quartz veins are located either at the walls of the early calcite veins that are  
388 re-opened, or in the core of the calcite veins propagating at the calcite crystal boundaries.  
389 Some quartz crystals are sheared which shows also the syn-kinematic character of these late  
390 silica precipitations. The study of the calcite cements present in the faults and open fractures  
391 of the Parras Basin reveals a homogeneously dull brown luminescence, and faint sector  
392 zoning under CL, only visible within some of the least deformed/sheared/crushed crystals.

393

394 *Clays.* XRD study has shown that a general process of clay transformation follows, from the  
395 top to the bottom of the Parras Basin, a general trend to illitization and chloritization of  
396 smectites, which is a very classic pattern of diagenetic transformation. Illite and chlorite are  
397 widespread in the Parras formation inside the study area. More specifically, it has been  
398 possible to demonstrate that diagenesis is not only influenced by the general conditions of  
399 temperature and pressure in relation to the sedimentary burial, but strain also plays a role on  
400 clay diagenesis. We observed that penetrative deformation process has the effect of  
401 accelerating the process of illitization and chloritization. Indeed, in the decollement zone,  
402 deformation was focused on surfaces of discontinuity corresponding to shear planes currently  
403 mineralized by calcite precipitation. Clay-rich portions between these shear planes are little  
404 deformed and mineralogical transformations are moderate. However, in the corridors of  
405 penetrative deformation (well-developed cleavage), mineralogical changes are intense and the  
406 vertical gradient of illitization is not respected anymore. In these areas, electronic microprobe  
407 mapping has shown that diagenesis is characterized by a strong illitization and chloritization  
408 of smectite, and jointly with an increase in the quartz content, and less calcite content  
409 compared to the clays-rich layers in the decollement zone (Fig. 22). This increase of  
410 diagenetic transformations in areas of penetrative deformation generates locally inverse  
411 gradients of illitization and chloritization. Such a feature is notably observed between the  
412 decollement zone and the cleavage corridors located above the decollement zone where  
413 deformation controls partly diagenesis (Fig. 22). Sample 65 in the lower zone is characterized  
414 by the presence of a large quantity of smectite and well-ordered illite-smectite interlayer  
415 visible with the presence of broad lines around 15 and 18 Å and the importance of the  
416 variations in line positions of the air dried (AD) and ethylen glycol (EG) profiles (blue and  
417 purple lines respectively and blue arrows to illustrate diffraction line displacements).. Sample  
418 63 in the intermediate zone is characterized by the presence of chlorite and illite and a small  
419 amount of illite-smectite interlayer visible with the presence of fine lines around 14, 10 and 7

420 Å and the small variation of positions of the lines of the AD and EG profiles (brown and red  
421 lines respectively). Sample 60 in the upper zone is characterized by the presence of chlorite  
422 and illite and a small amount of illite-smectite interlayer. The variation of the positions of the  
423 lines of the profiles AD and EG (green and orange lines respectively) is very small.

424 More generally, Scanning Electronic Microprobe study of scaly shale has shown that the  
425 initial fabric of their protolitic matrix does not show preserved stratigraphic layering. The  
426 only oriented fabric which is visible in the scaly shale corresponds to late microfractures in  
427 which calcite has precipitated. Clay minerals have recrystallized mainly to illite. Scattered  
428 patches of quartz and albite have also developed in the scaly shale (Fig. 23).

429

#### 430 *4.3. Fluid inclusion microthermometry and barometry*

431

432 The petrographic study of selected samples revealed that inclusions are present in calcite  
433 cements and in some cases in quartz cements (Fig. 24). Microthermometry measurements  
434 were performed on fluid inclusions trapped in these two types of minerals. It was possible to  
435 distinguish four types of fluid inclusions trapped in calcite or quartz minerals (Fig. S5, S6; in  
436 supplementary material): *Type 1* corresponds to isolated primary fluid inclusions dispersed in  
437 quartz and calcite minerals. They are sub-rectangular with dimensions ranging from 3 to 8 µm  
438 and they are all two-phase (liquid and vapor phases; Fig. 24). *Type 2* corresponds to primary  
439 fluid inclusions ranging from 3 to 8 µm in size with various shapes. These inclusions are  
440 single-phase gaseous inclusions and they look darker than the aqueous inclusions. These  
441 inclusions are present in calcite and quartz. *Type 3* corresponds to rectangular aqueous fluid  
442 inclusions aligned along calcite twins. These inclusions are late primary to secondary  
443 inclusions with dimensions between 2 and 5 µm. *Type 4* correspond to generally aligned  
444 secondary fluid inclusions (in fracture scar) of rectangular shape for the biggest and round for  
445 smaller. The rectangular inclusions have a size of about 2 to 3 µm and are most abundant.  
446 They are two-phase (liquid and vapor phase). Only primary inclusions of types 1 and 2 having  
447 a size greater than 3 µm were used for the microthermometry study presenter here.

448 Determining the first melting temperature ( $T_{fm}$ ) and the final melting temperature ( $T_{mi}$ ) of ice  
449 (low-temperature microthermometry) in the aqueous inclusions gives information on the  
450 composition of the fluid trapped in the inclusions and thus, for aqueous inclusions, the  
451 presence and the content of dissolved species. For all samples, first melting temperature ( $T_{fm}$ )  
452 values were obtained between -53° and -49°C (Table 1; Fig. S7 in supplementary material).  
453 These temperatures correspond to the eutectic temperature of a H<sub>2</sub>O-CaCl<sub>2</sub> system which is

454 consistent with the fact that the inclusions are present in carbonates (Bowers et., 1983).  
455 Temperatures of final melting ( $T_{mi}$ ) gave an estimate of the salinity of the fluid. In calcite,  $T_{mi}$   
456 display a wide range with statistical tendency towards a dominant window between  $-2^{\circ}\text{C}$  and  
457  $0^{\circ}\text{C}$  (Table 1; Fig. S8 in supplementary material). This suggests the presence of slightly saline  
458 water (Fisher, 1976). Eventually, this could be related to the presence dissolved  $\text{CO}_2$  in the  
459 inclusions which lower the melting point of water, but it was not possible to characterize the  
460 presence of clathrate in the inclusions. However, the small size of the inclusions is not  
461 favorable to identify the presence of  $\text{CO}_2$  clathrate. Values of  $T_{mi}$  slightly greater than  $0^{\circ}\text{C}$   
462 correspond probably to a metastable state of the fluid inclusions. Fluid inclusions in quartz  
463 have  $T_{mi}$  close to  $0^{\circ}\text{C}$  which is compatible with almost fresh water compositions. The  
464 homogenization temperatures ( $T_h$ ) observed in the liquid phase have been measured with an  
465 uncertainty of  $\pm 2^{\circ}\text{C}$  (Table 1; Fig. 24).  $T_h$  corresponds to the liquid-vapor transition.  
466 Considering the quite wide range of homogenization temperatures of the acquired distribution  
467 per samples, modal temperatures were chosen as references in the following discussion (Table  
468 1; Fig. S9 in supplementary material).  $T_h$  of primary fluid inclusions measured in the different  
469 samples range from  $125$  to  $185^{\circ}\text{C}$  in the calcite cements and reach maximum values of  $230^{\circ}\text{C}$   
470 in quartz cements.  $T_h$  evolves with the temperature of trapping. However,  $T_h$  are not necessary  
471 equal to trapping temperatures depending on the confining pressure. In samples 64A and 68A  
472 samples, trapping temperature was evaluated from cogenetic inclusions. Methane-rich  
473 inclusions were observed in samples collected in the decollement zone (samples 64A and  
474 68A). They have been observed in calcite and in quartz minerals. Methane can be identified  
475 by phase transition close and below critical temperature of  $-82^{\circ}\text{C}$ . For methane-rich  
476 inclusions, the  $T_h$  is between  $-92^{\circ}\text{C}$  and  $-94^{\circ}\text{C}$  (Fig. S10; in supplementary material). These  
477 inclusions were used to determine the temperature and pressure of trapping of the fluid in  
478 these samples (Mullis, 1979). The density has been determined from the saturation curve of  
479 methane (Hanor, 1980) and state equations MRK (Angus et al., 1978). The density values  
480 obtained from Angus' et al. (1978) model are  $0.292\text{ g/cm}^3$  at  $-92^{\circ}\text{C}$  and  $0.301\text{ g/cm}^3$  at  $-94^{\circ}\text{C}$ .  
481 This allowed us to draw methane isochores between  $50$  and  $300^{\circ}\text{C}$  (Setzmann and Wagner,  
482 1991) to determine the pressure within these inclusions for the  $T_h$  of the aqueous inclusions.  
483 The P-T conditions of the studied samples correspond to relatively high pressure and high  
484 temperature. In sample 68A, aqueous inclusions containing dissolved methane in HP-HT  
485 conditions, it can be considered that they are saturated with dissolved methane. Thus, in this  
486 case,  $T_h$  can be considered as equivalent to the temperatures of fluid trapping (Roedder and  
487 Bodnar, 1980; Roedder, 1984). The temperature and pressure conditions identified in the



488 sample 68A (Fig. 25) indicate that the fluids were trapped in the quartz crystal at a  
489 temperature of  $220 \pm 10^\circ\text{C}$  and pressure between 1380 and 1480 bars. In calcite, the trapping  
490 temperature is  $170 \pm 10^\circ\text{C}$  and pressure between 1200 and 1280 bars. Quartz forming later  
491 than calcite, it recorded higher temperatures due to a higher burial. These values show that  
492 calcite and quartz precipitated both in overpressure condition with a resulting increase of  
493 about  $26^\circ\text{C}$  per 100 bar between calcite and quartz precipitations following the isochores  
494 published by Setzmann and Wagner (1991; Fig. 25). In the other samples analyzed (107B,  
495 132, 83), in order to propose an approximation of the trapping temperatures as a function of  
496  $T_h$ , a correction was performed (Table 1) based on an estimate of the confining pressure of  
497 each sample deduced from an estimate of the erosion amount as summarized on the structural  
498 section of Fig. 6B and from the isochore curves of the  $\text{H}_2\text{O}-\text{CO}_2$  system (Fig. 25).

499

#### 500 *4.4. Isotopic analyses of carbonate cements*

501

502 Carbonate micrite matrix of samples of the group of Coahuila shown  $\delta^{18}\text{O}$  of about  $-10\text{‰}$   
503  $\text{vPDB}$  and slightly positive values for  $\delta^{13}\text{C}$   $\text{vPDB}$  (Table S<sub>II</sub>, in supplementary material).  
504 These measured values very probably reflect a thermal re-equilibration during burial of  
505 initially marine carbonates, which is consistent with the deep structural position of these  
506 carbonates (Fig. 65, 27). The analyzes of carbonate cements in the carbonate of the Coahuila  
507 group, in the decollement zone, in the carbonate pipes and in the veins of fractures within the  
508 sediments located above the decollement show very constant  $\delta^{18}\text{O}$  values and decreasing  
509  $\delta^{13}\text{C}$  values from the Coahuila carbonate rocks to rocks located above the decollement (Fig.  
510 26).  $\delta^{18}\text{O}$  and  $\delta^{13}\text{C}$  values of veins located above the decollement show a remarkable  
511 clustering, this regardless of the structural position and orientation of the fractures.  $\delta^{18}\text{O}$   
512 values are ranging between  $-9$  and  $-11\text{‰}$   $\text{vPDB}$  and  $\delta^{13}\text{C}$  values are ranging between  $-2$  and  $-$   
513  $6\text{‰}$   $\text{vPDB}$ . In these veins, the values of  $\delta^{18}\text{O}$  are fully comparable with those measured in the  
514 Coahuila carbonates. In contrast, values of  $\delta^{13}\text{C}$  are much lower in the calcite cements than in  
515 the carbonates of the Coahuila group, indicating enrichment in light carbon likely related to  
516 the influence of hydrocarbon-derived  $^{12}\text{C}$ . In addition, the isotopic values measured in  
517 cataclasites show significantly higher  $\delta^{18}\text{O}$  values than those measured in crystalline calcites.  
518 The few samples showing very low values in  $\delta^{13}\text{C}$  ( $-10$  to  $-11\text{‰}$   $\text{vPDB}$ ) correspond to  
519 cements that delivered hydrocarbon inclusions.

520

521 *4.5. Rock-Eval 6 analyses*

522

523 In rock Eval 6 pyrolysis technique, the hydrocarbons liberated during the progressive heating  
524 are measured with a FID detector (Flame Ionization Detector) and form the peak S1  
525 (representing the free thermo-vaporized hydrocarbons) and the peak S2 (products of pyrolysis  
526 during cracking of organic matter). In the studied samples, the peaks S1 are either nil or very  
527 low (probably remaining traces of hydrocarbon gas). S2 peaks are also very low, hardly  
528 measurable in the Cerro Grande formation and in the Canon del Tulle formation (Table SII, in  
529 supplementary material).  $T_{max}$  is a function of the maximum temperature of the S2 peak and it  
530 corresponds to a maturity index of organic matter. We obtained  $T_{max}$  values of 460°C in the  
531 Cerro Grande formation and between 483 and 495°C in in the Canon del Tulle formation,  
532 which correspond to high maturities of organic matter (gas window). In the Parras Shale  
533 formation, S2 and so  $T_{max}$  are not measurable ( $T_{max} > 500^{\circ}\text{C}$ ; equivalent to  $V_{Ro} > 1.7\%$ )  
534 instead of the presence of residual carbon (Table SII, in supplementary material), which is  
535 characteristic of very high maturities (overmature organic matter). The residual carbon  
536 constitutes most of the total organic content in all the studied samples. Therefore, these data  
537 have shown that the organic matter which is in the Parras shale is the gas window or  
538 overmature in the whole study area. This demonstrates that gas has been generated in the  
539 Parras shale of the studied area.

540

541 *4.6. Raman spectroscopy (RSCM geothermometer)*

542

543 The temperatures obtained by the RSCM method in scaly ‘mobile’ shale rocks just above the  
544 decollement zone and in the core of the main folds (samples 8B, 11, 120C, 113; location in  
545 Fig. 6A) gave values in the range  $180\text{-}220\pm 10^{\circ}\text{C}$  (Fig. S11 in supplementary material). These  
546 results are consistent with those obtained using Rock-Eval techniques and from the study of  
547 fluid inclusions in quartz which very probably crystalized during the thermal peak. Notably,  
548 sample 120C (north of sample 68A; Fig. 6A) gave RSCM temperature of  $220\pm 10^{\circ}\text{C}$  and  
549 similar temperature deduced from fluid inclusions in quartz in sample 68A. The thermal peak  
550 measured within the ‘mobile’ shale inside the core of the large folds gave RSCM  
551 temperatures between  $180$  and  $190\pm 10^{\circ}\text{C}$  (samples 8A, 11 and 113; Fig. 6).

552

553 *4.7. Thermal modeling*

554

555 Temperature is a parameter which evolves directly with burial and uplift during tectonic  
556 events. The thermal model used in this study simulates the stratigraphic back-stripping and  
557 the tectonic thickening and subsequent uplift history (Fig. 28). To fit the model with the  
558 paleothermometric results, notably the peak temperatures in specific formations which were  
559 estimated by fluid inclusions in quartz crystals and RSCM method in shale in the decollement  
560 zone, we had to choose a heat flow  $50 \text{ mW/m}^2$  at the base of the section taking an average  
561 constant surface temperature of  $20^\circ\text{C}$ . Modeling results suggest a significant temperature  
562 increase in the Coahuila and Parras formations during the compressive tectonic phase which is  
563 responsible for the decollement within the Parras shale. The model shows that the thermal  
564 peak occurred just after fault activity (during late Paleocene times) and reaches about  $180^\circ\text{C}$   
565 at the top of the of Parras formation and  $240$  to  $250^\circ\text{C}$  at the top of the Coahuila carbonates  
566 (Fig. 28). These results concerning the timing of the temperature peak are in good agreement  
567 with those of the study of Gray et al. (2001) from apatite fission track and apatite helium  
568 dating made at a regional scale.

569

## 570 **5. Interpretation**

571

572 This study of a wide scale tectonic wedge affected by a major decollement located in a shale-  
573 rich formation has shown that this system evolved through different steps as summarized in  
574 Figs. 29 and 30. Combined studies including field geology, XRD, SEM, microthermometry  
575 and barometry on fluid inclusions, isotopic study of carbonates, Rock-Eval and RSCM  
576 measurements and thermal modeling made possible to identify the following major stages  
577 concerning the history of deformation - fluid migration - diagenesis relationships of the site  
578 studied which probably occurred during a progressive continuum of deformation.

579

580 *Stage A: Early diagenesis related to sedimentation.* During the deposition of the deltaic  
581 system, the early stages of diagenesis were characterized by a transitional transformation of  
582 clays, from the top to the base of the delta system, with illitization and chloritization of  
583 smectite (mainly genesis of interlayered illite-smectite). Such trend was observed all over the  
584 study area (Fig. 6). The development of syn-compaction sedimentary dikes probably occurred  
585 during this initial stage of diagenesis.

586

587 *Stage B: Scaly shale and early folds.* The older compressive deformations affecting shale  
588 rocks have generated a penetrative scaly fabric within parts of the Parras shale formation. We

589 consider these layers as comparable to what is commonly considered as mobile shale. Most of  
590 the penetrative deformation was observed in areas which are very poor in sandstone layers. In  
591 areas containing numerous sandstone horizons (even thin), folds and fractures were observed  
592 but no evidence for penetrative deformation. Penetrative deformation developed essentially in  
593 the inner part of the study area (southern part), in the shale located today immediately above  
594 the basal decollement or in the core of the large folds. The penetrative deformation of shale  
595 occurred in the domain of transformation of smectite to illite and hydrocarbon gas generation  
596 (Fig. 29, 30). This penetrative deformation is not always located in the same stratigraphic  
597 horizon (Fig. 6B, 7). This process initiated the structure of the core of the major folds made of  
598 deformed shale with stretched and discontinuous sandstone beds inside. In the inner part of  
599 the study area (the deepest part during deformation), large tectonic accumulations of  
600 deformed clay-rich material can be regarded as detachment folds. It was found that there were  
601 both, spatial and temporal evolutions of the rheology of the shale-rich layers; the rheological  
602 behavior of shale varied over time (unlike decollement in evaporites for example) and  
603 penetrative deformation was localized in certain preferred areas (as opposed also to evaporite  
604 levels in which the deformation is much more distributed).

605  
606 *Stage C: Decollement propagation and deep fluid flow.* Within the clay-rich formation that  
607 hosts the decollement, the deformed shale observed above the decollement zone and in the  
608 core of the folds did not act, neither in time nor in space, with a uniform constant rheology.  
609 Indeed, deformation mechanisms in shale evolved over time. Clearly an evolution of the  
610 deformation mechanisms occurred from a penetrative ductile process to a brittle behavior  
611 (faulting overimposed on early penetrative deformation). This event corresponds to the period  
612 of development of the carbonate pipes which are interpreted as former fluid conduits  
613 comparable to similar structures described in different places (Deville et al., 2006; 2020; De  
614 Boever et al., 2006; Nyman et al., 2010; Conti et al., 2014; Zwicker et al., 2015; Tamborrino  
615 et al., 2019). This event corresponds also to the period of development of the syn-kinematic  
616 calcite veins. We interpret this fracturing and diagenetic stage as related to high fluid pressure  
617 at the base of the system (see results of the study of fluid inclusions, Fig. 29) and associated to  
618 a sudden and massive flow of fluids from below what is today the decollement level (fluids  
619 issued from the carbonates of the Coahuila group). The widespread lack of CL zonation, with  
620 only a very faint sector zoning preserved locally, suggests that large calcite crystals have  
621 quickly precipitated and are co-genetic (same fluids that have filled the various fractures).  
622 This suggests that these fluids have a common origin, the most likely source of calcite being

623 located in the upper part of the Cretaceous carbonates (Coahuila group). The massive  
624 precipitation of large calcite crystals in fractures is probably due to the migration of fluids  
625 from the carbonates of the Coahuila group (or at least buffered with these carbonates). The  
626 isotopic study of calcite veins as shown that  $\delta^{18}\text{O}$  are very constant in the carbonate rocks of  
627 the Coahuila group, in the decollement zone, in the carbonate pipes and in the veins of  
628 fractures within the sediments located above the decollement (Fig. 26). This directly suggests  
629 that calcite precipitated in similar temperature conditions in all these locations and that the  
630 precipitation of the calcite veins above the decollement did not happened in thermal  
631 equilibrium with the host rocks (similar temperature conditions whatever is their structural  
632 position and higher temperature conditions compared to cataclasites; e.g. hydrothermal-type  
633 fluids; Figs. 26, 27, 28). Considering the syn-kinematic characters of the calcite precipitations  
634 at the decollement level, these fluids have obviously circulated at the base of the deltaic  
635 system, at the beginning of the decollement processes. It is thus considered that the beginning  
636 of the compressive decollement tectonics in shale was marked by a widespread fracturing  
637 process (hydraulic fractures) at the base of the deltaic system and at the top of the underlying  
638 carbonates, which is consistent with the high overpressure conditions (Figs. 29, 30) deduced  
639 from the fluid inclusion study and the burial estimate deduced from field observation (Fig.  
640 6B) and from the backstripping approach (Fig. 28A). Overpressure rise is related to  
641 conjugated effects of fluid retention within the shale-rich environment and pressure  
642 generation mainly related to clay dehydration and smectite to illite transformation coupled  
643 with hydrocarbon gas generation. These fracturing processes were probably the consequence  
644 of a major tectonic thickening in the innermost areas (south of the Parras Basin and Sierra  
645 Madre). The tectonic thickening was probably at the origin of the development of  
646 overpressure in the outer areas, at the deformation front and the increase of pressure has been  
647 high enough to generate natural hydraulic fracturing processes. The consequence of this  
648 episode of fracturing was an important flow of fluids from the Cretaceous carbonates of the  
649 Coahuila group located below the decollement level. Calcite precipitations associated with  
650 this flow of dissolved carbonate-rich fluids were found mostly at the base of the deltaic  
651 system (upper part of the Parras shale formation and Cerro del Pueblo formation). These  
652 fluids have circulated widely at least at the beginning of the decollement tectonics. According  
653 to microthermometric results and modeling, these fluids have circulated rapidly since these  
654 hot fluids were not in thermal equilibrium with their host rocks during in the precipitation of  
655 carbonates in the fractures, as confirmed by the modeled burial history. It is also important to  
656 note that some areas (including the decollement zone) were also associated with hydrocarbon

657 migration during this episode of fluid migration. The decollement propagated upward in the  
658 stratigraphic series toward the tectonic front.

659

660 *Stage D: Development of cataclasites.* The generation of the cataclasites corresponds to a  
661 mechanical damage of the previously precipitated calcite cements associated with faulting.  
662 Subsequent to the precipitation of calcite in the fractures, these cements have been  
663 tectonically damaged, partly crushed. This process has generated locally cataclasite breccias  
664 including polygenic elements. This event was associated with the recrystallization of calcite  
665 cements, as indicated by significantly higher  $\delta^{18}\text{O}$  values than those measured in calcite spars.  
666 These values directly suggest lower temperatures of recrystallization than those of the  
667 crystalline calcite (see above). If we assume that the recrystallization took place in a closed  
668 environment, without the contribution of renewed external fluids, and that the only fluids  
669 available were issued from local pressure-solution during cataclasis, recrystallization  
670 temperatures can be estimated using a classical fractionation diagram (Fig. 27). The  $\delta^{18}\text{O}$  of  
671 the calcite spars and the  $T_h$  measured in fluid inclusions constrain the range of the isotopic  
672 compositions of the parent fluids for these calcites between +7‰ and +13‰ (Fig. 27), which  
673 is a typical range for basinal evolved fluids. Cataclastic deformations within residual trapped  
674 fluids of these compositions, and/or within fluids issued from local pressure-solution  
675 associated to these deformation processes at crystal/crystal boundaries (or crystal fragment  
676 boundaries), may thus indicate that cataclasite could have formed in a temperature range of  
677 110°C to 160°C (Fig. 27). It is likely that these lower temperatures correspond to those of the  
678 host rocks that correspond to the local geothermal conditions at this time (Fig. 28).

679

680 *Stage E: Hydraulic closure of the thrust system.* While early syn-kinematic diagenetic events  
681 show evidence of fluid migration from below the decollement level, late syn-kinematic  
682 diagenetic events are characterized mainly by quartz precipitation. It can be considered that  
683 during the evolution of decollement tectonics, the system tended to be isolated from the  
684 influence of dissolved carbonate-rich fluids from depth (from below the decollement zone)  
685 and only silica-rich fluids were responsible for the diagenetic processes. We interpret this  
686 diagenetic stage as reflecting a form of closure of the system and that silica results from local  
687 fluid circulation only issued from either sandstone or clays located above the decollement.  
688 The common localization of these silica cements at the periphery of claystone host fragments  
689 suggests most probably that clay-rich material is at the origin of quartz precipitation probably  
690 during smectite-illite transformation processes (Fig. 21). Indeed, during burial, with the

691 increase of temperature, smectite is transformed into illite with the incorporation of K,  
692 sometimes Al, and the release of silica, diverse ions ( $\text{Na}^{2+}$ ,  $\text{Ca}^{2+}$ ,  $\text{Mg}^{2+}$ ,  $\text{Fe}^{2+/3+}$ , ...) and water.  
693 Finally, at the end of the period of decollement tectonics, the system located above the  
694 decollement level was most probably isolated from fluid migration from below the  
695 decollement (closed system). This late stage of thrust tectonics was also characterized by the  
696 thermal peak corresponding to the maximum burial. It was also marked by the development of  
697 cleavage bands which have favored clay transformations inducing coupled processes between  
698 deformation and clay diagenesis.

699

## 700 **6. Discussion about shale mobility**

701

702 The tectonic evolution of this case study can be compared with mechanical experiments made  
703 on shale rocks. Increasing importance of shale of deep hydrocarbon exploration targets but  
704 also gas/oil shale plays exploration led to improve the knowledge about the rheological  
705 properties of shale at depth. Series of geomechanical experiments have shown that, in absence  
706 of significant overpressure, the strength of shale rocks increases with depth before reaching  
707 the transition from brittle to ductile behavior which appears at relatively moderate depth  
708 compared to sandstone and carbonate (Nygard et al., 2006; Jaeger et al., 2007; Fjaer et al.,  
709 2008; Strozyk and Tankiewicz, 2014; Gale et al., 2014; Ge et al., 2015; Holt et al., 2015).  
710 The lower is the sandstone fraction in shale, the more ductile the shale (Wang et al., 2015;  
711 Labani and Rezaee, 2015). The transition between brittle and ductile is gradual. Notably,  
712 Rybacki et al. (2015; 2016) and Yuan et al. (2017) have shown that the brittle-ductile  
713 transition in shale occurs currently at a depth between 4 and 5 km. Indeed, critical confining  
714 stress of brittle-ductile transition has been estimated to be above 70 MPa (Yuan et al., 2017).  
715 For instance, if we consider an average density of  $2.6 \text{ g/cm}^3$  for a shale-rich sedimentary  
716 column, this is equivalent to a depth of about 4400 m. Indeed, in natural cases, thick shale-  
717 rich tectonic wedges have a visco-elastic behavior below 5 km, as it has been evidenced from  
718 the geometrical relaxation after a major earthquake (Peterson et al., 2018). Most of the authors  
719 consider that the increase of fluid pressure favour the brittle behaviour of rocks associated  
720 with the decrease of effective stress (Hubbert and Willis, 1957; Hubbert and Rubey, 1959;  
721 Davis et al., 1983; Dahlen et al., 1984; Day-Stirrat et al., 2010, and many others). Indeed, if  
722 geomechanical experiments have demonstrated that normally compacted or moderately over-  
723 consolidated shale show ductile response to increasing load, on the other side, it has been  
724 shown that overpressure build-up turn shale into over-consolidated material which show

725 brittle behavior during loading (Nygard et al., 2006; Yuan et al., 2017). Shale tectonic  
726 processes observed during this study are consistent with these later mechanical experiments.  
727 In the case study presented here, it has been shown that after a brittle behavior during  
728 sedimentation (stage A, characterized notably by fractures injected by sand), an early phase of  
729 compressive deformation was characterized by ductile deformation of shale in the lower parts  
730 of the tectonic wedge (stage B, Figs. 29, 30). This ductile deformation of shale predated high  
731 overpressure conditions during which, finally, brittle deformation prevailed during the  
732 overpressure peak (stage C, Figs. 29, 30). The estimated depth where early ductile  
733 deformation was prevailing is around 5 km (Fig. 28), which is equivalent to what was  
734 obtained in mechanical experimental results (Yuan et al., 2017). The domain of ductile  
735 deformation of shale is within the domain of illization of smectite and hydrocarbon gas  
736 generation (thermal cracking of organic matter in the gas window; Fig. 28). Concerning the  
737 propagation of the decollement, it has long been shown that a decollement corresponds to an  
738 interface with a low coefficient of friction between two fragile levels along which  
739 displacement can be initiated by excess fluid pressure (Hubbert and Rubey, 1959). In  
740 compressive domains with high differential stress, when the fluid pressure excess is high, it is  
741 able to produce rupture associated with shearing (Grauls, 1999) which makes possible the  
742 activity of a decollement. This is indeed what has been observed in this case study where it  
743 has been characterized that the decollement was mostly active during the maximum  
744 overpressure period (Figs. 29, 30). With a significant excess of pressure, the stresses tend,  
745 over geological times, to be carried gradually by both the solid but also by the fluid inducing a  
746 tendency towards a stress-fluid pressure coupling (Tingay et al., 2003) and fractures occur  
747 when high pressure excess overtakes the minimum stress plus tension strength. This is indeed  
748 the type of conditions observed at the decollement level in the case studied where the shale  
749 sediments, after being deformed ductily, have been affected by fractures injected with fluids,  
750 associated with massive calcite precipitation (Figs. 10, 16). The study of fluid inclusions  
751 coupled with modeling has shown that the decollement zone at that time reached  
752 hydrofracturing pressure conditions (Figs. 28, 29). Similarly, below the decollement, notably  
753 in the carbonates of the Coahuila arch, rocks show evidence of massive fracturing processes  
754 generating open fractures which have been cemented by single phase calcite cement (Fig. 9B).  
755 These processes are interpreted as a result of hydraulic fracturing which is perfectly consistent  
756 with the results of the fluid inclusion study and modeling showing that the fracturing  
757 processes below the decollement and the decollement activity associated with the massive



758 calcite precipitation event occurred in the required conditions for hydraulic fracturing (Figs.  
759 28, 29).

760 It was also shown that, although shale behaves locally in a ductile way, no evidence for  
761 piercing ductile shale was encountered through the overlying stratigraphic layers (as it is  
762 common in salt tectonics). Also, no evidence for liquefaction has been found, except the  
763 development of few sedimentary dikes in the innermost part of the study area corresponding  
764 to sand mobilization associated with migration of early fluids. During compressive  
765 deformation, sedimentary mobilization was only observed as cataclastic injection in fault  
766 planes (stage D). From the results of this study, the absence of massive liquefaction process  
767 demonstrates that shale tectonics clearly differs from mud volcanism processes which are a  
768 consequence of a reaction chain of fluid migration and not a direct mobilization of shale from  
769 depth (Deville, 2009; Deville et al., 2010).

770

## 771 **7. Conclusion**

772

773 The area studied is a rare outcropping terrestrial analogue illustrating deformation processes  
774 which occur at depth, in thick sedimentary thrust wedges associated with major decollement  
775 situated in overpressured shale. It offers outcropping conditions over large areas which made  
776 possible a series of different observations and analytical approaches which have shown  
777 notably the following points: Massive volumes of deformed shale with scaly fabric, disrupted  
778 stratification and boudinage of the sandstone beds are present close to the decollement and in  
779 the core of the larger folds. This process of deformation occurred only in the deepest parts of  
780 the thrust wedge (below a depth of about 5 km) in the domain of transformation of smectite  
781 into illite and hydrocarbon gas generation. The structure of these shale-rich bodies result from  
782 very penetrative, distributed deformation (ductile mode of deformation). We interpret these  
783 deformed shale-rich sediments as outcropping analogs of deformed sedimentary bodies  
784 described as mobile shale at depth on many seismic data all over the world. The deformation  
785 mechanisms in these mobile shale-rich units evolved over time from penetrative deformation  
786 (scaly fabric and cleavage) to localized brittle deformation (faulting) but the deformation  
787 mechanism evolved also laterally in the same formation depending probably on the pressure  
788 conditions. As such, both temporal and spatial evolution of the rheology of shale was deduced  
789 from our observation. More generally, these results suggest that it is possible to define an  
790 ephemeral window where shale is prone to behave in a ductile way below the shale brittle-  
791 ductile transition (depth of about 4-5 km) and above high overpressure reaching processes of

792 hydraulic-driven rupture. The brittle deformation was interpreted from the fluid inclusion  
793 study as associated to high overpressure close to hydraulic fracturing condition. Also, it is  
794 worth noting that the beginning of the decollement tectonics was associated with a percolation  
795 of fluids from below the decollement and this process was progressively blocked during  
796 deformation without influence from fluid issued from below the decollement (evolution from  
797 an open system to a closed system).

798

### 799 **Acknowledgements**

800

801 Thanks are due to TOTAL SA (DBR project) for financial support. Thanks are also due to  
802 Nicole Guihlaumou for her help in the work of Clement Dutranoy concerning the fluid  
803 inclusions study and to Emily Albouy, Stéphane Raillard and Nadine Ellouz who took part in  
804 field-trips in the Parras Basin. Thanks are also due to Michael Joachimski from the University  
805 of Erlangen for carbonate isotopic analyses. We thank also the reviewers for their constructive  
806 contributions to improve the form of the initial manuscript.

807

808 This paper is dedicated to the memory of Marc Tardy.

809  
810  
811  
812  
813  
814  
815  
816  
817  
818  
819  
820  
821  
822  
823  
824  
825  
826  
827  
828  
829  
830  
831  
832  
833  
834  
835  
836  
837  
838  
839  
840  
841  
842  
843  
844  
845  
846  
847  
848  
849  
850  
851  
852  
853  
854  
855  
856  
857  
858

## References

- Angus S., Armstrong B., de Reuck K., 1978. International Thermodynamic Tables of the fluid state: Methane. Pergamon, Oxford.
- Bartolini, C., Montana, C., Mickus, K., 1995. Geological structure of the Parras Basin-Sierra Madre Oriental area, north-central Mexico utilizing geophysical data. In: AGU 1995 fall meeting. Eos, Transactions, American Geophysical Union. 76, 46, Suppl., 535-536.
- Bartolini, C., Mickus, K., 2001. Tectonic blocks, magmatic arcs, and oceanic terrains, a preliminary interpretation based on gravity, outcrop, and subsurface data, Northeast-central Mexico. The western Gulf of Mexico basin, tectonics, sedimentary basins, and petroleum systems. Bartolini Claudio, ed, Buffler Richard T, ed, Cantu Chapa Abelardo, ed. AAPG Mem. 2001, 75, 29-43.
- Beysac, O., Goffe, B., Chopin, C., Rouzaud, J.-N., 2002. Raman spectra of carbonaceous material in metasediments: a new geothermometer. *J. Metamorph. Geol.*, 20, 859–871. <https://doi.org/10.1046/j.1525-1314.2002.00408.x>
- Bowers, T.S., Helgeson, H.C., 1983. Calculation of the thermodynamic and geochemical consequences of nonideal mixing in the system H<sub>2</sub>O-CO<sub>2</sub>-NaCl on phase relations in geologic systems: Equation of state for H<sub>2</sub>O-CO<sub>2</sub>-NaCl fluids at high pressures and temperatures. *Geochimica et Cosmochimica Acta*, 47, 7, 1247-1275. [https://doi.org/10.1016/0016-7037\(83\)90066-2](https://doi.org/10.1016/0016-7037(83)90066-2)
- Bradshaw, B.E., Watkins, J.S., 1994. Growth-fault evolution in offshore Texas. *Gulf Coast Association of Geological Societies Transactions*, 44, 103–110.
- Briggs, S.E., Davies, R.J., Cartwright, J.A., Morganz, R., 2006. Multiple detachment levels and their control on fold styles in the compressional domain of the deepwater west Niger Delta. *Basin Research* 18, 435–450, <https://doi.org/10.1111/j.1365-2117.2006.00300.x>
- Brown, K.M., 1990. The nature and hydrologic significance of mud diapirs and diatremes for accretionary systems. *Journal of Geophysical Research*, 95, 8969-8982.
- Bruce, C., 1973, Pressured shale and related sediment deformation: mechanism for development of regional contemporaneous faults. *AAPG Bulletin*, 57, 878–886.
- Cohen, H.A., McClay, K., 1996. Sedimentation and shale tectonics of the northwestern Niger Delta front. *Marine and Petroleum Geology*, 313–328, [https://doi.org/10.1016/02648172\(95\)00067-4](https://doi.org/10.1016/02648172(95)00067-4)
- Conti, S., Fontana, D., Lucente, C.C., Pini, G.A., 2014. Relationships between seep-carbonates, mud volcanism and basin geometry in the Late Miocene of the northern Apennines of Italy: the Montardone mélange. *Int. J. Earth Sci.* 103, 281–295. <https://doi.org/10.1007/s00531-013-0928-y>
- Corredor, F., Shaw, J.H., Bilotti, F., 2005. Structural styles in the deep-water fold and thrust belts of the Niger Delta. *AAPG Bulletin*, 89, 753–780, <https://doi.org/10.1306/02170504074>
- Davis, D., Suppe, J., Dahlen, F.A., 1983. The mechanics of fold and thrust belts. *Journal of Geophysical Research*, 88, 1153-1172.
- Dahlen, F.A., Suppe, J., Davis D., 1984. Mechanics of fold-and-thrust belts and accretionary wedges: cohesive Coulomb theory. *Journal of Geophysical Research*, 89, 10 087-10 101.
- Day-Stirrat, R.J., McDonnell, A., Wood, L.J., 2010. Diagenetic and seismic concerns associated with interpretation of deeply buried "mobile shales," in L. Wood, ed., *Shale tectonics*. AAPG Memoir, 93, 5–27.
- De Boever, E., Huysmans, M., Muchez, P., Dimitrov, L., Swennen, R., 2009. Controlling factors on the morphology and spatial distribution of methane-related tubular concretions – case study of an Early Eocene seep system. *Mar. Pet. Geol.* 26, 1580–1591. <https://doi.org/10.1016/j.marpetgeo.2008.11.004>.

- 859 Deville, É., Battani, A., Griboulard, R., Guerlais, S., Herbin, J.P., Houzay, J.P., Muller, C.,  
860 Prinzhofer, A., 2003. Mud volcanism origin and processes: New insights from Trinidad  
861 and the Barbados Prism. Special publication of the Geological Society (London) on  
862 Subsurface Sediment Mobilisation. Van Rensbergen, P., Hillis, R.R., Maltman, A.J., &  
863 Morley, C.K. (eds), 216, p. 475-490. <https://doi:10.1.1.896.2623>
- 864 Deville, É., Guerlais, S-H., Callec, Y., Lallemand, S, Noble, M., Schmitz, J. and the  
865 CARAMBA research team, 2006. Liquefied vs. stratified subsurface sediment  
866 mobilization processes: insight from the south of the barbados accretionary prism.  
867 *Tectonophysics*, 428, 33-47. <https://doi.org/10.1016/j.tecto.2006.08.011>
- 868 Deville É., 2009. Mud volcano systems. Nova Publishers, *Volcanoes: Formation, Eruptions*  
869 *and Modelling*, Chapter 6. Neil Lewis and Antonio Moretti (eds), Nova Science Pub.  
870 Inc., 95-126.
- 871 Deville É., Guerlais S-H., Lallemand S., Schneider F., 2010. Fluid dynamics and subsurface  
872 sediment mobilization processes: An overview from the south-eastern Caribbean. *Basin*  
873 *Research*, Special issue on fluid flows and Subsurface Sediment Remobilization, 22,  
874 361–379, <https://doi.org/10.1111/j.1365-2117.2010.00474.x>
- 875 Deville É., Scalabrin, C., Jouet, G., Cattaneo, A., Battani, A., Noirez, S., Vermesse, H., Olu,  
876 K., Corbari, L., Boulard, M., Marsset, T, Dall’asta, M., Torelli, M, Pastor, L., Pierre, D.,  
877 Loubrieu, B., 2020. Fluid seepage associated with slope destabilization along the Zambezi  
878 Margin (Mozambique). *Marine Geology* 428, 106275.  
879 <https://doi.org/10.1016/j.margeo.2020.106275>
- 880 Eberth, D.A., Delgado-de Jesus, C.R., Lerbekmo, J.F., Brinkman, D.B., Rodriguez de la Rosa,  
881 R.A., Sampson, S.D., 2004. Cerro del Pueblo Fm (Difunta Group, Upper Cretaceous),  
882 Parras Basin, southern Coahuila, Mexico: reference sections, age and correlation. *Revista*  
883 *Mexicana de Ciencia Geologicas* 21, 2, 335-352.
- 884 Elsley, G.R., Tieman, H., 2010. A comparison of prestack depth and prestack time imaging of  
885 the Paktoa complex, Canadian Beaufort MacKenzie Basin, in L. Wood, ed., *Shale*  
886 *tectonics*. AAPG Memoir 93, 79–90.
- 887 Fisher, J.R., 1976. The volumetric properties of H<sub>2</sub>O. A graphical portrayal. *J. Res. Us Geol.*  
888 *survey*, 4, 189-193.
- 889 Fjaer, E., Holt, R.M., Horsrud, P., Raaen, A.M., Risnes, R., 2008. *Petroleum related rock*  
890 *mechanics*, 2nd ed. Elsevier, Amsterdam, 491 p.
- 891 Gale, J.F.W., Laubach, S.E., Olson, J.E., 2014. Natural fractures in shale: a review and new  
892 observations. *AAPG Bull.* 98, 11, 2165–216. <https://doi:10.1306/08121413151>
- 893 Ge, H, Yang, L, Shen, Y, Wu, S., 2015. Experimental investigation of shale imbibition  
894 capacity and the factors influencing loss of hydraulic fracturing fluids. *Pet. Sci.* 12, 4,  
895 636–650. <https://doi:10.1007/s12182-015-0049-2>
- 896 Goldstein, R.H., 2001. Fluid inclusions in sedimentary and diagenetic systems. *Lithos* 55, p.  
897 159-193. [https://doi.org/10.1016/S0024-4937\(00\)00044-X](https://doi.org/10.1016/S0024-4937(00)00044-X)
- 898 Grauls, D., 1999. Overpressure: causal mechanism, conventional and hydromechanical  
899 approaches. *Oil Gas Sci. Technol.*, 54, 667-678.  
900 <https://doi.org/10.2516/ogst:1999056>
- 901 Gray, G.G., Pottorf, R.J., Yurewicz, D.A., Mahon, K.I., Pevear, D.R., Chuchla, R.J., 2001.  
902 Thermal and chronological record of syn-to post-Laramide burial and exhumation, Sierra  
903 Madre Oriental, Mexico. The western Gulf of Mexico basin, tectonics, sedimentary  
904 basins, and petroleum systems. Bartolini Claudio, ed, Buffler Richard T, ed, Cantu chapa  
905 Abelardo, ed. AAPG Memoir, 75, 159-181.
- 906 Hanor, J.S., 1980. Dissolved methane in sedimentary brines: potential effect on the PVT  
907 properties of fluid inclusions. *Econ. Geol.* 75, 603-609.

908 Holt, RM, Fjær, E, Stenebraten, JF, Ness, O.M., 2015. Brittleness of shales: relevance to  
909 borehole collapse and hydraulic fracturing. *Journal of Petroleum Science and Engineering*  
910 131, 200–209. <https://doi:10.1016/j.petrol.2015.04.006>

911 Hooker, J.N., Larson, T.E., Eakin, A., Marrett, R., 2015. Fracturing and fluid flow in a sub-  
912 decollement sandstone; or, a leak in the basement. *Journal of the Geological Society* 172,  
913 4, 428-442. <https://DOI:10.1144/jgs2014-128>

914 Hubbert M.K., Willis, D.G., 1957. Mechanics of hydraulic fracturing. *Transactions of the*  
915 *American Institute of Mining, Metallurgical, and Petroleum Engineers*, 210, 153–68.

916 Hubbert, M.K., Rubey, W.W., 1959. Role of fluid pressure in mechanics of overthrust  
917 faulting: I. Mechanics of fluid-filled porous solids and its application to overthrust  
918 faulting. *Geological Society of America Bulletin*, 70, 115–66.

919 Huh, S., Watkins, J.S., Bradshaw, B.E., Xi, J., Kasande, R., 1996. Regional structure and  
920 stratigraphy of the Texas shelf, Gulf of Mexico. *AAPG Bulletin*, 80, 1504–1535.

921 Ifrim, C., Stinnesbeck, W., Espinosa, B., Ventura, J.F. 2015. Upper Campanian (Upper  
922 Cretaceous) cephalopods from the Parras Shale near Saucedas, Coahuila, Mexico. *Journal*  
923 *of South American Earth Sciences*, 64, 229-257.

924 Jaeger, J.C., Cook, N.G.W., Zimmerman, R.W., 2007. *Fundamentals of rock mechanics*, 4th  
925 ed. Blackwell, Oxford, 468 p.

926 Labani, M.M., Rezaee, R., 2015. The importance of geochemical parameters and shale  
927 composition on rock mechanical properties of gas shale reservoirs: a case study from the  
928 Kockatea Shale and Carynginia Formation from the Perth Basin, Western Australia. *Rock*  
929 *Mech Rock Eng.* 48, 3, 1249–1257. <https://doi:10.1007/s00603-014-0617-6>

930 Lafargue, E., Marquis, F., Pillot, D., 1998. Rock-Eval 6 applications in hydrocarbon  
931 exploration, production, and soil contamination studies. *Revue de l'Institut Français du*  
932 *Pétrole* 53, 4, 421-437.

933 Lahfid A., Beyssac O., Deville E., Negro F., Chopin C., Goffé B., 2010. Evolution of the  
934 Raman spectrum of carbonaceous material in low-grade metasediments of the Glarus  
935 Alps (Switzerland). *Terra Nova*, 22, 354–360. [https://doi:10.1111/j.1365-](https://doi:10.1111/j.1365-3121.2010.00956.x)  
936 [3121.2010.00956.x](https://doi:10.1111/j.1365-3121.2010.00956.x)

937 Lawton, T.F., Giles, K.A., Vega, F.J., Rosales, D.C., 2001. Stratigraphy and origin of the La  
938 Popa Basin, Nuevo Leon and Coahuila, Mexico. *The western Gulf of Mexico basin,*  
939 *tectonics, sedimentary basins, and petroleum systems* Bartolini Claudio, ed, Buffler  
940 Richard T, ed, Cantu chapa Abelardo, ed. *AAPG Memoir*, 75, 219-240.  
941 <https://doi.org/10.1306/M75768C9>

942 Lehmann, C., Osleger, D.A., Montañez, I.P., Sliter, W., Arnaud-Vanneau, A., Banner, J.  
943 1999. Evolution of Cupido and Coahuila carbonate platforms, early Cretaceous,  
944 northeastern Mexico. *GSA Bulletin*, 111, 7, 1010-1029.

945 Lindholm, R.C., Finkelman, R.B., 1972. Calcite staining: semiquantitative determination of  
946 ferrous iron. *J. Sedim. Petrol.* 42, 239-242. [https://doi:10.1306/74D724FA-2B21-11D7-](https://doi:10.1306/74D724FA-2B21-11D7-8648000102C1865D)  
947 [8648000102C1865D](https://doi:10.1306/74D724FA-2B21-11D7-8648000102C1865D)

948 Machel, H.G., 2000. Application of cathodoluminescence to carbonate diagenesis. In Pagel  
949 M., Barbin V., Blanc P.& Ohnenstetter D., *Cathodoluminescence in Geosciences.*  
950 Springer-Verlag, Berlin, 271-301.

951 Martínez-Díaz, J.L., Aguillón-Martínez, M.C., Luque, J., Vega, F.J. 2017. Paleocene decapod  
952 Crustacea from northeastern Mexico: Additions to biostratigraphy and diversity. *Journal*  
953 *of South American Earth Sciences*, 74, 67-82.

954 McBride, E.F., Weidie, A.E., Wolleben, J.A., 1971. Deltaic origin of Difunta group (late  
955 Cretaceous to Paleocene), Parras Basin, Coahuila and Nuevo Leon, Mexico. *AAPG*  
956 *Bulletin.* 55, 2, 352.

- 957 McBride, E.F., Wolleben, J.A, Weidie, A.E. 1973. Deltaic and Associated Facies of Difunta  
958 Group (Late Cretaceous - Paleocene), Parras and La Popa basins, Coahuila and Nuevo  
959 Leon, Mexico. AAPG Bulletin. 57, 9, 1833-1834.
- 960 Mc Bride, E.F., Weidie, A.E., Wollenben, J.A., Laudon, R.C., 1974. Stratigraphy and  
961 structure of the Parras and La Popa Basins, northeastern Mexico. Geological Society of  
962 America Bulletin, 84, 1603-1622.
- 963 McBride, E.F., 1974. Significance of color in red, green, purple, olive, brown, and gray beds  
964 of Difunta Group, northeastern Mexico. Journal of Sedimentary Petrology. 44, 3, 760-  
965 773.
- 966 McBride, E.F., Weidie, A.E, Wolleben, J.A., 1975. Deltaic and associated deposits of Difunta  
967 Group (late Cretaceous to Paleocene), Parras and La Popa basins, northeastern Mexico.  
968 In: Deltas, models for exploration. Broussard Martha Lou (editor). 485-522. Houston  
969 Geol. Soc.. Houston, United States.
- 970 Morley, C.K., 2003. Mobile shale related deformation in large deltas developed on passive  
971 and active margins. Geological Society (London) Special Publication 216, p. 335–357.
- 972 Morley, C.K., Guerin, G., 1996. Comparison of gravity driven deformation styles and  
973 behavior associated with mobile shales and salt. Tectonics, 15, 1154–1170,  
974 <https://doi.org/10.1029/96TC01416>
- 975 Mullis J. 1979. The system methane-water as a geologic thermometer and barometer from the  
976 external part of the central Alps. Bull. Soc. Fr. Minerall. Cristallogr. 102, 526-536.
- 977 Murray G.E, Weidie A.E Jr., Boyd D.R, Forde R.H, Lewis P.D Jr. 1962. Formational  
978 divisions of Difunta Group, Parras Basin, Coahuila and Nuevo Leon, Mexico. AAPG  
979 Bulletin. 46, 3, 374- 383.
- 980 Murray, G.E., Boyd, D., Durham, C.O Jr., Forde, R.H, Lawrence, R.M, Lewis, P.D Jr.,  
981 Martin, K.G, Wolleben, J.A, Weidie, A.E, Wilbert, W.P., 1960. Stratigraphy of Difunta  
982 Group, Parras Basin, States of Coahuila and Nuevo Leon, Mexico. Session - International  
983 Geological Congress. Part 5, 82-96.
- 984 Murray G.E., Boyd D.R., Wilson J.A., Wolleben J.A. 1960. Late Cretaceous fossil locality,  
985 eastern Parras Basin, Coahuila, Mexico. Journal of Paleontology. 34, 2, 368-370.
- 986 Murray G.E., Wolleben J.A, Boyd D.R. 1959. Difunta strata of Tertiary age, Coahuila,  
987 Mexico. 1959. AAPG Bulletin. 43, 10, 2493-2495.
- 988 Nyman, S.L., Nelson, C.S., Campbell, K.A., 2010. Miocene tubular concretions in East Coast  
989 Basin, New Zealand: Analogue for the subsurface plumbing of cold seeps. Mar. Geol.  
990 272, 319–336. <https://doi.org/10.1016/j.margeo.2009.03.021>
- 991 Nygard, R., Gutierrez, M., Bratli, R.K., Høeg, K., 2006. Brittle–ductile transition, shear  
992 failure and leakage in shales and mudrocks. Marine and Petroleum Geology, 23, 201–  
993 212. <https://doi.org/10.1016/j.marpetgeo.2005.10.001>
- 994 O'neil, J.R., Clayton, R.N., Mayeda, T.K., 1969. Oxygen isotope fractionation in divalent  
995 metal carbonates. J. Chem. Physics, 51, 5547-5558.
- 996 Machel, H.G., 2000. Application of cathodoluminescence to carbonate diagenesis. In Pagel,  
997 M., Barbin, V., Blanc, P., Ohnenstetter D., Cathodoluminescence in Geosciences.  
998 Springer-Verlag, Berlin, 271-301.
- 999 Peterson, K. E., Barnhart, W. D., Li, S. 2018. Viscous accretionary prisms: Viscoelastic  
1000 relaxation of the Makran accretionary prism following the 2013 Baluchistan, Pakistan  
1001 earthquake. Journal of Geophysical Research: Solid Earth, 123.  
1002 <https://doi.org/10.1029/2018JB016057>.
- 1003 Rybacki, E., Reinicke, A., Meier, T., Makasi, M., Dresen, G., 2015. What controls the  
1004 mechanical properties of shale rocks? – Part I: Strength and Young's modulus.  
1005 Brittleness. Journal of Petroleum Science and Engineering 135, 702–722.  
1006 <https://doi.org/10.1016/j.petrol.2015.10.028>

- 1007 Rybacki, E., Meier, T., Dresen, G., 2016. What controls the mechanical properties of shale  
1008 rocks? – Part II: Brittleness. *Journal of Petroleum Science and Engineering* 144, 39–58.  
1009 <http://dx.doi.org/10.1016/j.petrol.2016.02.022>
- 1010 Roedder, E., Bodnar, R.J., 1980. Geological pressure determinations from fluid inclusion  
1011 studies. *Ann. Rev. Earth Planet. Sci.* 8, 263-301.
- 1012 Roedder, E. 1984. Fluid inclusions. Mineralogical Society of America. *Rev. Mineralogy*, 12,  
1013 644 p.
- 1014 Setzmann, U., Wagner, W., 1991. A new equation of state and tables of thermodynamic  
1015 properties for methane covering the range from melting line to 625 K at pressures up to  
1016 1000 Mpa. *J. Phys. Chem. Ref. Data* 20, 1061-115.
- 1017 Shepherd, T., Rankin, A.H., Altderton, D.H.M., 1985. A practical guide to fluid inclusion  
1018 studies. In Blackie (Ed.), Chapman et Hall. New York, 239 p.
- 1019 Soegaard, K., Ye, H., Halik, N., Daniels, A.T., Arney, J., Garrick, S., 2003. Stratigraphic  
1020 evolution of Latest Cretaceous to early Tertiary Difunta foreland basin in northeast  
1021 Mexico: Influence of salt withdrawal on tectonically induced subsidence by the Sierra  
1022 Madre Oriental fold and thrust Belt, in C. Bartolini, R.T. Buffler, and J. Blickwede, eds.,  
1023 *The Circum-Gulf of Mexico and the Caribbean: Hydrocarbon habitats, basin formation,*  
1024 *and plate tectonics: AAPG Memoir* 79, 364-394.
- 1025 Strozyk J, Tankiewicz M. The undrained shear strength of overconsolidated clays. *Procedia*  
1026 *Eng.* 91, 317–321. <https://doi.org/10.1016/j.proeng.2014.12.067>
- 1027 Tamborrino, L., Himmler T., Elvert M., Conti S., Gualtieri A., Fontana D., Bohrmann G.  
1028 2019. Formation of tubular carbonate conduits at Athina mud volcano, eastern  
1029 Mediterranean Sea. *Marine and Petroleum Geology* 107, 20-31.  
1030 <https://doi.org/10.1016/j.marpetgeo.2019.05.003>
- 1031 Tardy, M, Ramirez, R.C, Patino, A.M., 1975. El frente de la napa de Parras (conjunto Cadena  
1032 Alta-Altiplano central) en el area de Aramberri, N. L., Sierra Madre Oriental, Mexico.  
1033 *Revista -Instituto de Geologia.* 2, Universidad Nacional Autonoma de Mexico, Instituto  
1034 de Geologia. Mexico, D.F., Mexico, 1-11.
- 1035 Tardy, M., 1980. Contribution a l'étude geologique de la Sierra Madre Oriental du Mexique:  
1036 Tesis doctoral, Université Pierre et Marie Curie de Paris, 445 p.
- 1037 Tingay, M., Hillis, R., Morley, C., Swarbrick, R., Okpere, E., 2003. Pore pressure/stress  
1038 coupling in Brunei Darussalam - implications for shale injection. in P. Van Rensbergen,  
1039 R. R Hillis, A.J. Maltman & C.K. Morley (eds), *Subsurface Sediment Mobilization.* 369-  
1040 379. Geological Society of London. <https://10.1144/GSL.SP.2003.216.01.24>.
- 1041 Van Rensbergen, P., Morley, C.K., 2000. 3D seismic study of a shale expulsion syncline at  
1042 the base of the Champion Delta, offshore Brunei and its implications for the early  
1043 structural evolution of large delta systems: *Marine and Petroleum Geology*, v. 17, p. 861–  
1044 872, doi:[10.1016/S02648172\(00\)00026-X](https://doi.org/10.1016/S02648172(00)00026-X).
- 1045 Van Rensbergen, O., Hillis, R. R., Maltman, A. J., Morley, C. K., 2003a. Subsurface sediment  
1046 mobilization: Introduction, in P. Van Rensbergen, R. R. Hillis, A. J. Maltman, and C. K.  
1047 Morley, eds., *Subsurface sediment mobilization: Geological Society (London) Special*  
1048 *Publication* 216, 1–8.
- 1049 Van Rensbergen, P., and C. K. Morley, 2003b, Re-evaluation of mobile shale occurrences on  
1050 seismic sections of the Champion and Baram deltas, offshore Brunei: *Geological Society*  
1051 *(London) Special Publication*, p. 395–409.
- 1052 Vega, F.J., Ahyong, S.T., Espinosa, B., Flores-Ventura, J., Luna, L., González-González,  
1053 A.H. 2018. Oldest record of Mathildellidae (Crustacea: Decapoda: Goneplacoidea)  
1054 associated with Retroplumidae from the Upper Cretaceous of NE Mexico. *Journal of*  
1055 *South American Earth Sciences* 82, 62-75. <https://doi.org/10.1016/j.jsames.2017.12.002>

1056 Vogt, M., Stinnesbeck, W., Zell, P., Kober, B., Kontny, J., Herzer, N., Frey, E., Rivera-Sylva,  
1057 H.E., Padilla Gutierrez, J.M., Amezcua, N., Huerta, D.F., 2016. Age and depositional  
1058 environment of the "dinosaur graveyard" at Las Águilas, southern Coahuila, NE Mexico.  
1059 *Palaeogeography, Palaeoclimatology, Palaeoecology*, 441, 758-769.  
1060 <https://doi.org/10.1016/j.palaeo.2015.10.020>

1061 Wachter, E., Hayes, J.M., 1985. Exchange of oxygen isotopes in carbon-dioxide - phosphoric  
1062 acid systems. *Chemical Geology* 52, 365-374. [https://doi.org/10.1016/0168-](https://doi.org/10.1016/0168-9622(85)90046-6)  
1063 [9622\(85\)90046-6](https://doi.org/10.1016/0168-9622(85)90046-6)

1064 Wang, D., Ge, H., Wang, X., 2015. A novel experimental approach for fracability evaluation  
1065 in tight-gas reservoirs. *J. Nat. Gas Sci. Eng.* 23, 239–249.  
1066 <https://doi.org/10.1016/j.jngse.2015.01.039>

1067 Warning, K.R, McBride, E.F., 1976. Transgressive-regressive deposits of Difunta Group  
1068 (upper Cretaceous-Paleocene), Parras Basin, Mexico. *AAPG Bulletin* 60, 4, AAPG-  
1069 SEPM annual meeting, 732.

1070 Weidie, A.E. Murray, G.E, Cameron, C.P, Long, J.J. Jr., Ritchie, E.J., 1966. Stratigraphy and  
1071 structure of Parras Basin and adjacent areas of northeastern Mexico. *AAPG Bulletin* 50,  
1072 3, 639-640.

1073 Weidie, A.E., Murray, G.E., 1967. Geology of Parras Basin and adjacent areas of northeastern  
1074 Mexico. *AAPG Bulletin* 51, 5, 678-695.

1075 Weidie, A.E., Wolleben, J.A, McBride, E.F., 1978. Geologic framework of northeastern  
1076 Mexico. In: *Minas de Golondrinas and Minas Rancherías, northeastern Mexico.* 27-38.

1077 Wiener, R.W., Mann, M.G., Angelich, M.T., Molyneux, J.B., 2010. Mobile shale in the Niger  
1078 Delta: Characteristics, structure, and evolution, in Wood, ed., *Shale tectonics.* AAPG  
1079 *Memoir* 93, 145–160.

1080 Wolleben, J.A., 1977. Paleontology of the Difunta Group (Upper Cretaceous-Tertiary) in  
1081 northern Mexico. *Journal of Paleontology* 51, 2, 373-398.  
1082 <http://www.jstor.org/stable/1303616>

1083 Wood, L., 2010. Shale tectonics: A preface. In L. Wood, ed, *Shale tectonics; AAPG Memoir*  
1084 *93*, 1-4. <https://DOI:10.1306/13231305M93730>

1085 Wood, L., 2012. Shale tectonics. In Wood, L., 2012. *Shale tectonics.* In *Phanerozoic Passive*  
1086 *Margins, Cratonic Basin and Global tectonic Map.* 43-54. [https://DOI:10.1016/B978-0-](https://DOI:10.1016/B978-0-444-56357-6.00002.0)  
1087 [444-56357-6.00002.0](https://DOI:10.1016/B978-0-444-56357-6.00002.0)

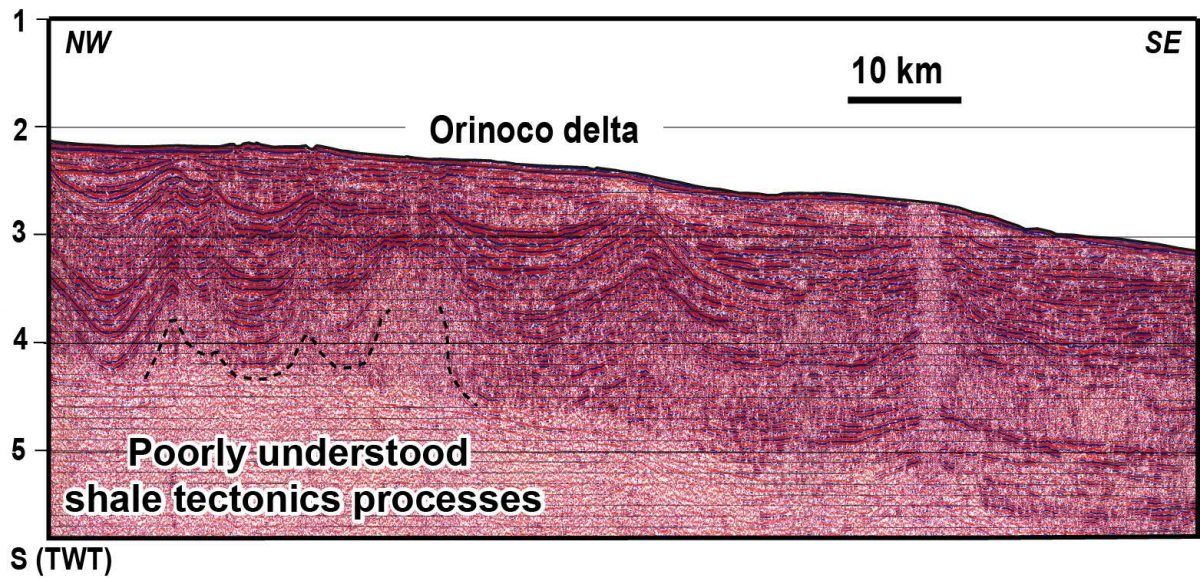
1088 Yuan, Y-S., Jin, Z-J., Zhou, Y., Liu, J-X., Li, S-J., Liu, Q-Y., 2017. Burial depth interval of  
1089 the shale brittle–ductile transition zone and its implications in shale gas exploration and  
1090 production. *Pet. Sci.* 14, 637–647. <https://DOI:10.1007/s12182-017-0189-7>

1091 Zwicker, J., Smrzka, D., Gier, S., Goedert, J.L., Peckmann, J., 2015. Mineralized conduits are  
1092 part of the uppermost plumbing system of Oligocene methane-seep deposits, Washington  
1093 State (USA). *Mar. Pet. Geol.* 66, 616–630. [https://doi.org/10.1016/j.](https://doi.org/10.1016/j.marpetgeo.2015.05.035)  
1094 [marpetgeo.2015.05.035](https://doi.org/10.1016/j.marpetgeo.2015.05.035)  
1095



1096 **FIGURES**

1097

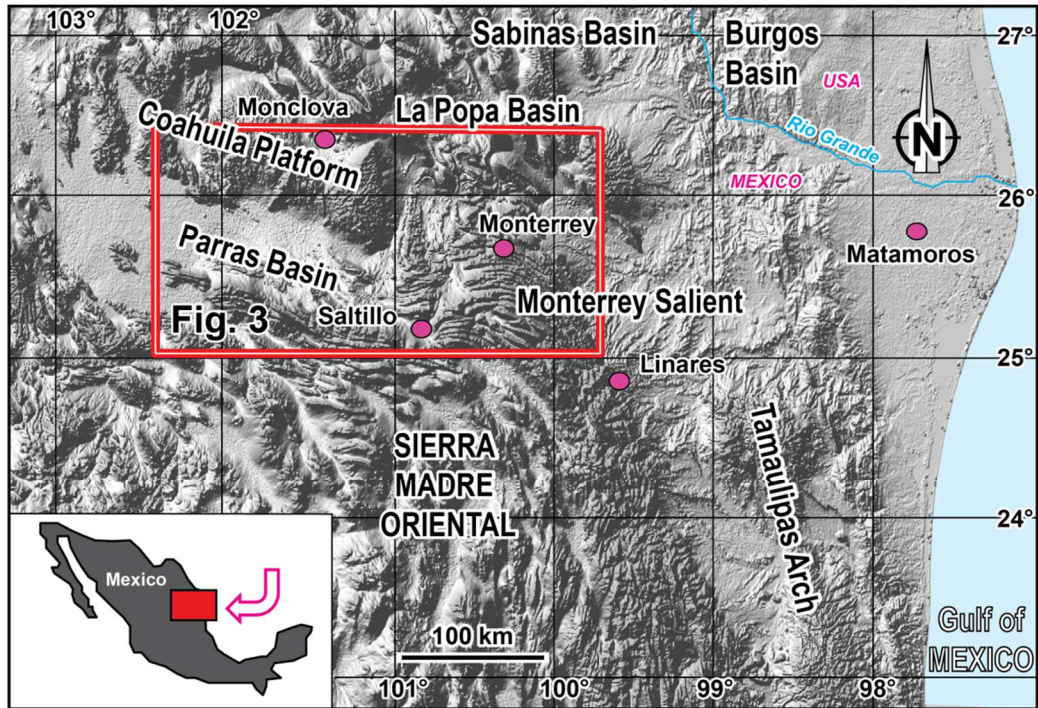


1098

1099

1100 **Fig. 1.** A typical example of a seismic line from the Orinoco delta – Barbados accretionary  
1101 prism junction (modified from Deville et al., 2010) showing shale tectonics features at depth,  
1102 as observed on seismic reflection data in many areas of the world.

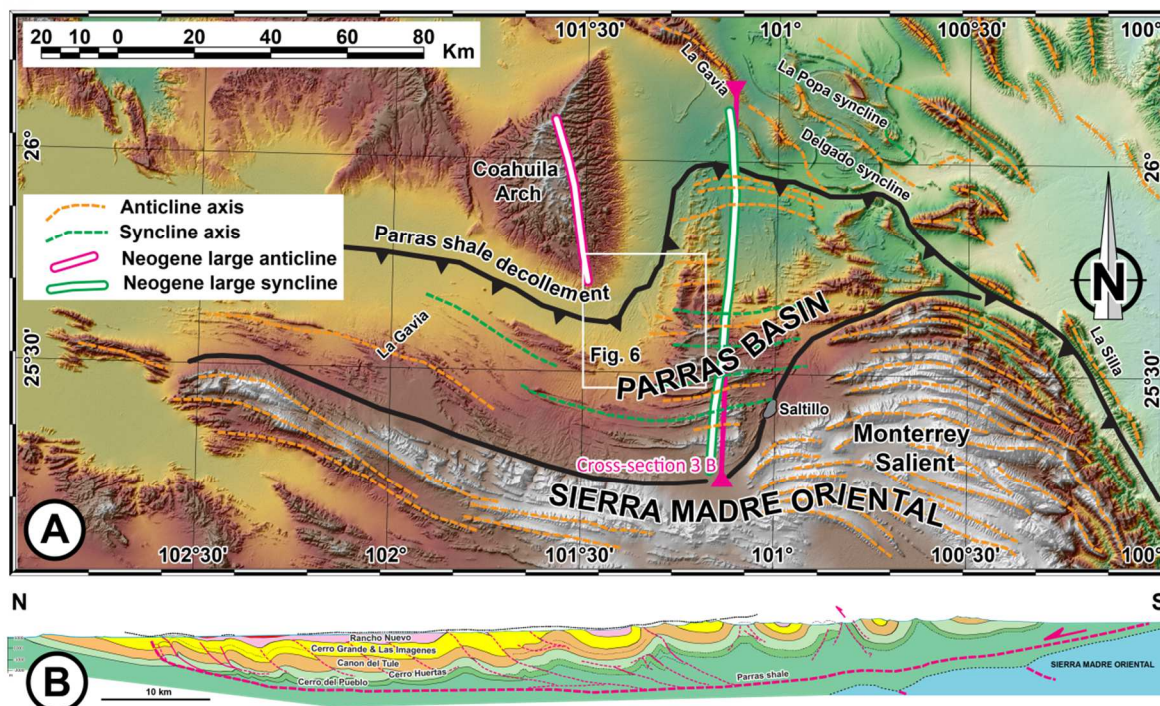
1103



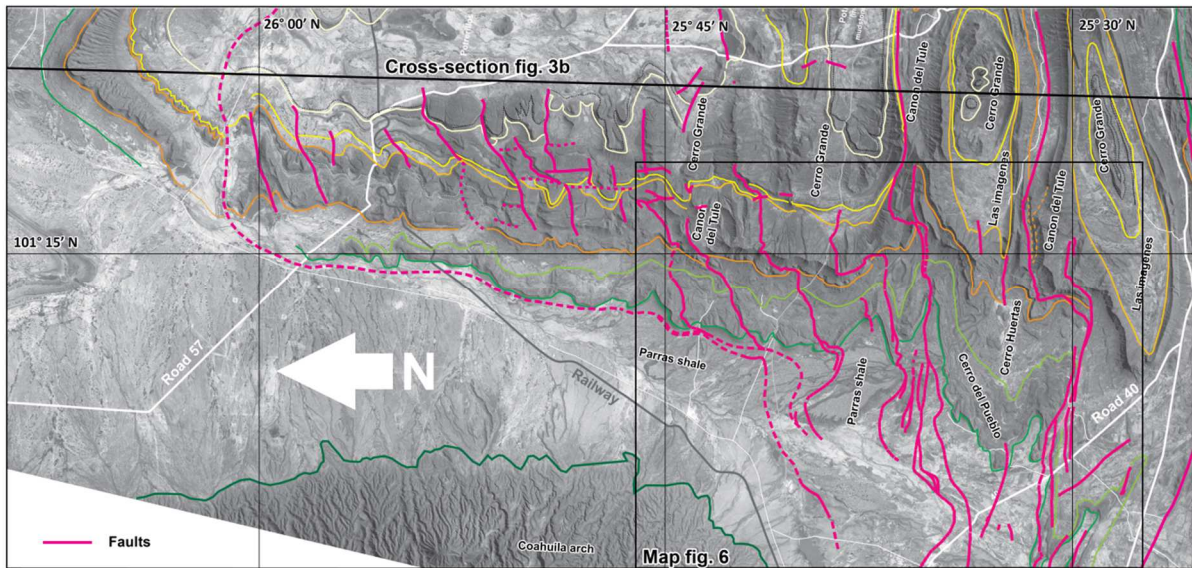
1104  
 1105  
 1106  
 1107

**Fig. 2.** Location of the study area in north-eastern Mexico (DEM downloaded from <https://lpdaacsvc.cr.usgs.gov>).

1108  
1109  
1110

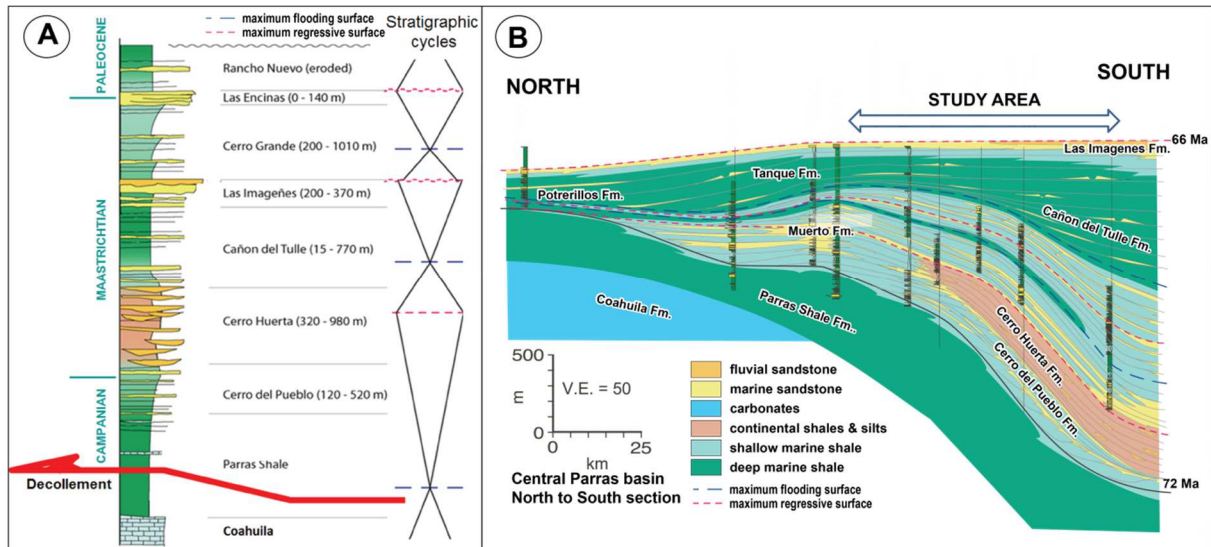


1111  
1112 **Fig. 3.** Structural sketch-map (A) and geological section (B) of the study area (No vertical  
1113 exaggeration).



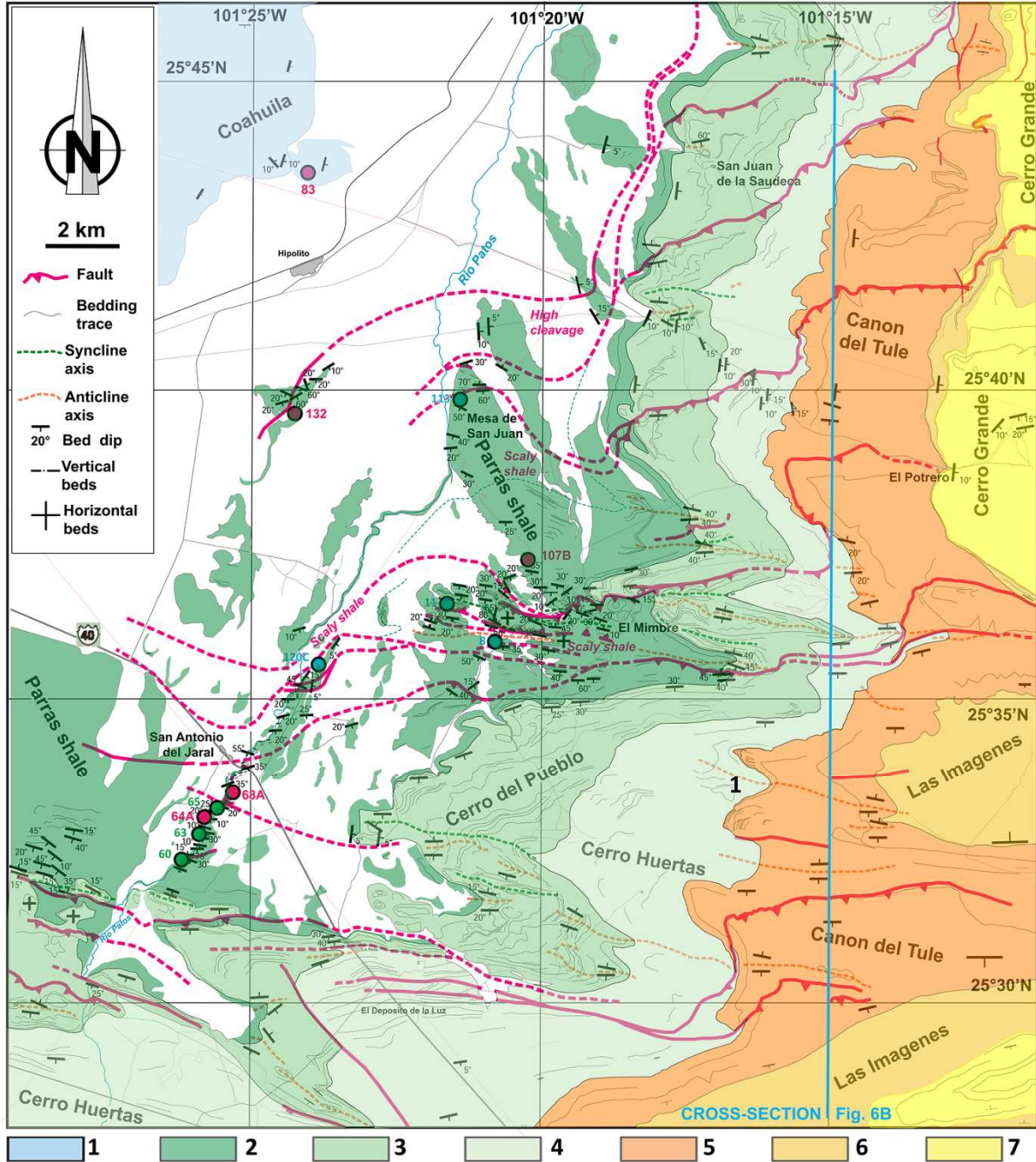
1114  
 1115  
 1116  
 1117  
 1118  
 1119

**Fig. 4.** Satellite image (Lansat) covering the study area. Because of the uplift of the Coahuila Arch to the west and because of the uplift-related erosion of Campanian-Maastrichtian layers, present-day outcrops in this area illustrates directly the structure of the Parras compressive structures (as an initial cross-section before the uplift), allowing direct observations and rock sampling all over the cross-section.



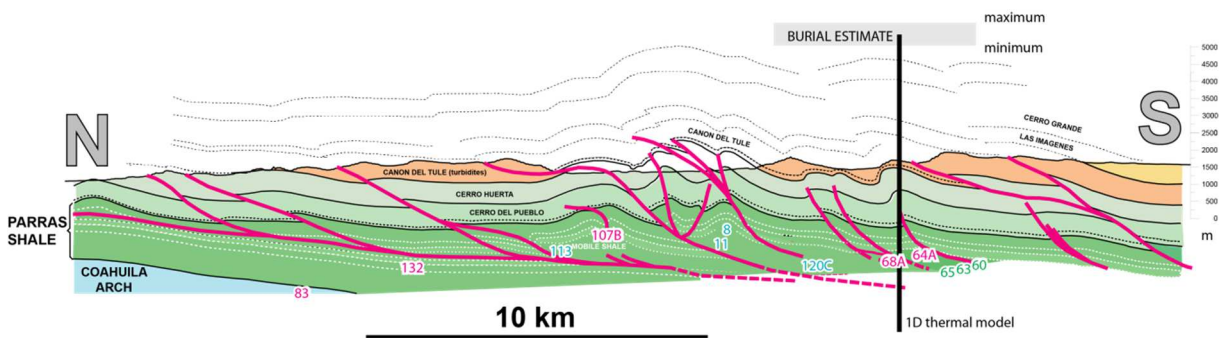
1120  
 1121  
 1122  
 1123  
 1124  
 1125  
 1126  
 1127

**Fig. 5.** **A.** Simplified stratigraphic column of the Parras Basin (not at scale). **B.** Facies correlation of sedimentologic sections in the central Parras Basin (compilation of field works by Soegaard et al., 2003 and this study; detailed stratigraphic logs are from Soegaard et al., 2003).



1129  
1130  
1131

**A**

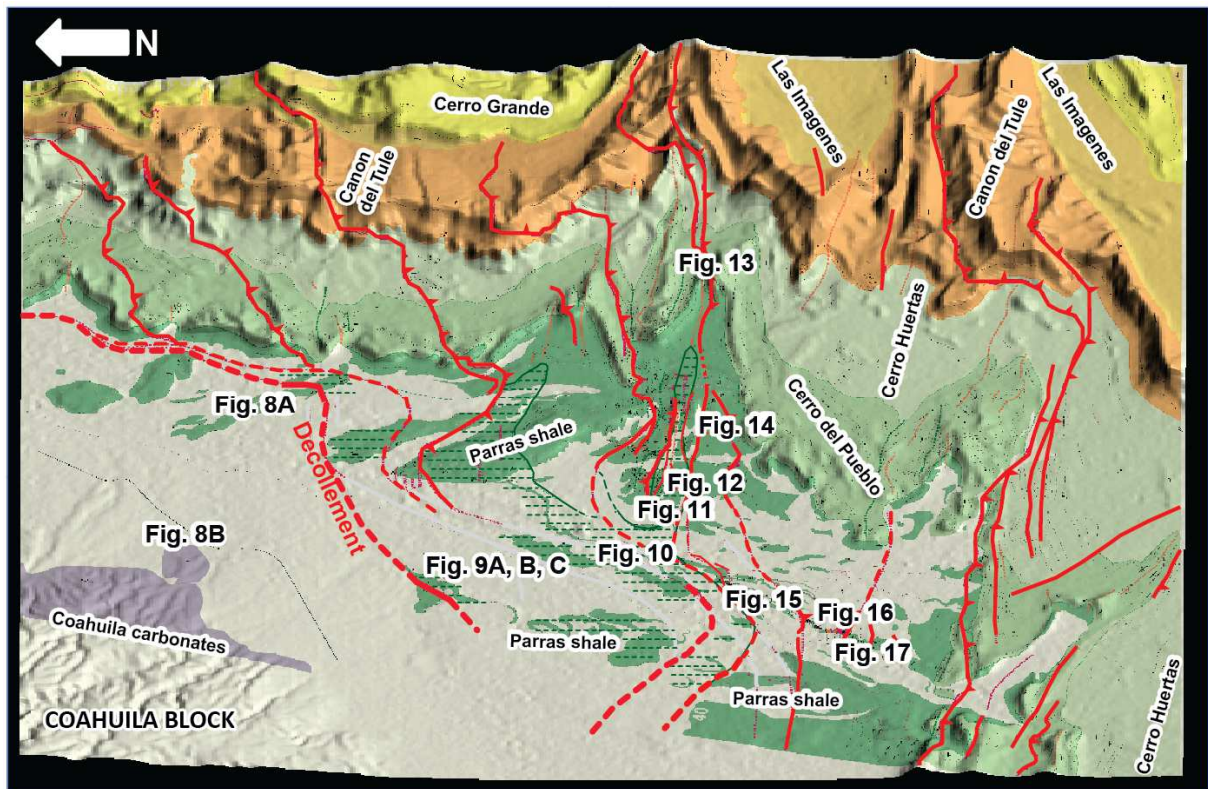


1132  
1133

**B**

1134  
1135  
1136  
1137  
1138  
1139

**Fig. 6. A.** Geological map in the area of San Antonio del Jaral and Hipolito (Location in Fig. 3); 1. Carbonate of the Coahuila group; 2. Parras shale formation; 3. Cerro de Pueblo formation; 4. Cerro Huertas formation; 5. Canon del Tule formation; 6. Las Imagenes formation; 7. Cerro Grande formation (see ages and description in the text). **B.** Geological cross-section with location of the 1D thermal model presented in Fig. 28.



1140  
 1141  
 1142  
 1143  
 1144  
 1145  
 1146

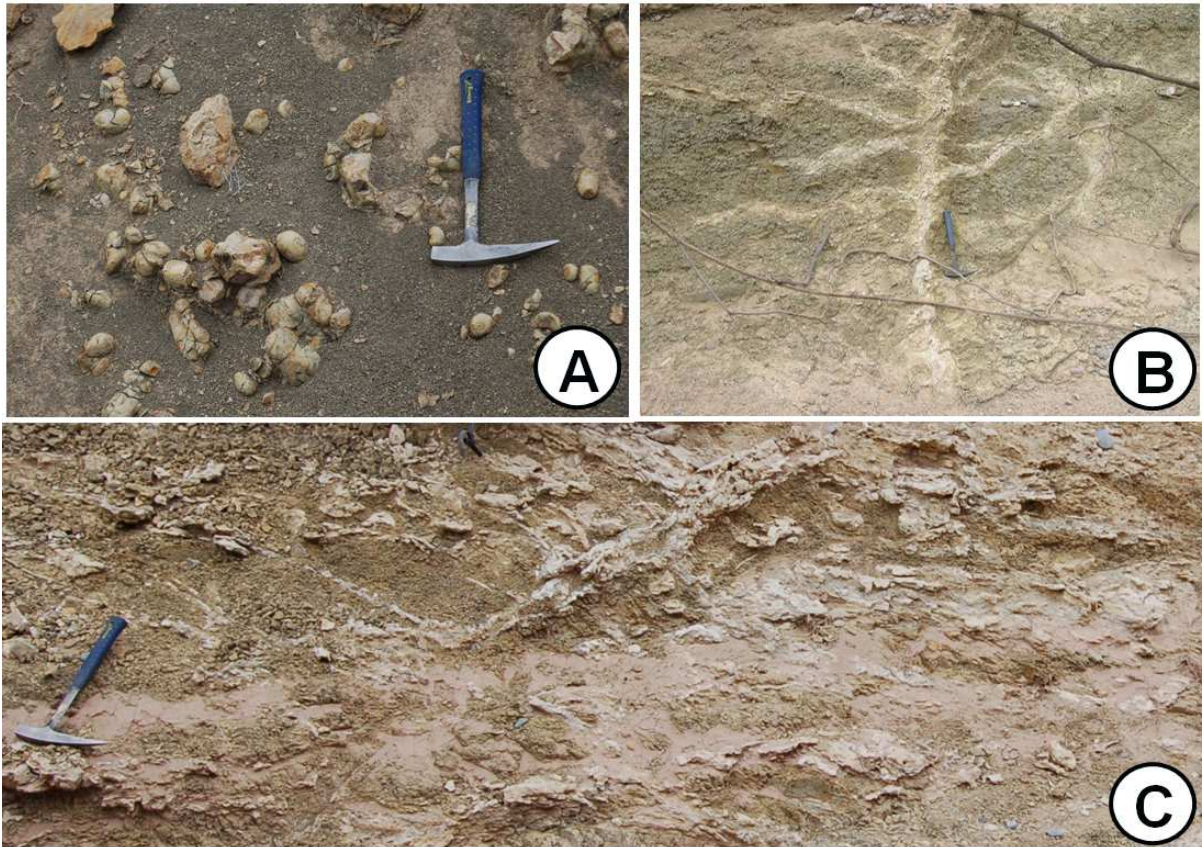
**Fig. 7.** Structural block diagram with location of the photographs of Figs. 8, 9, 10, 11, 12, 13, 14, 15, 16, and 17. Doted-lines within the Parras shale correspond to scaly shale areas.





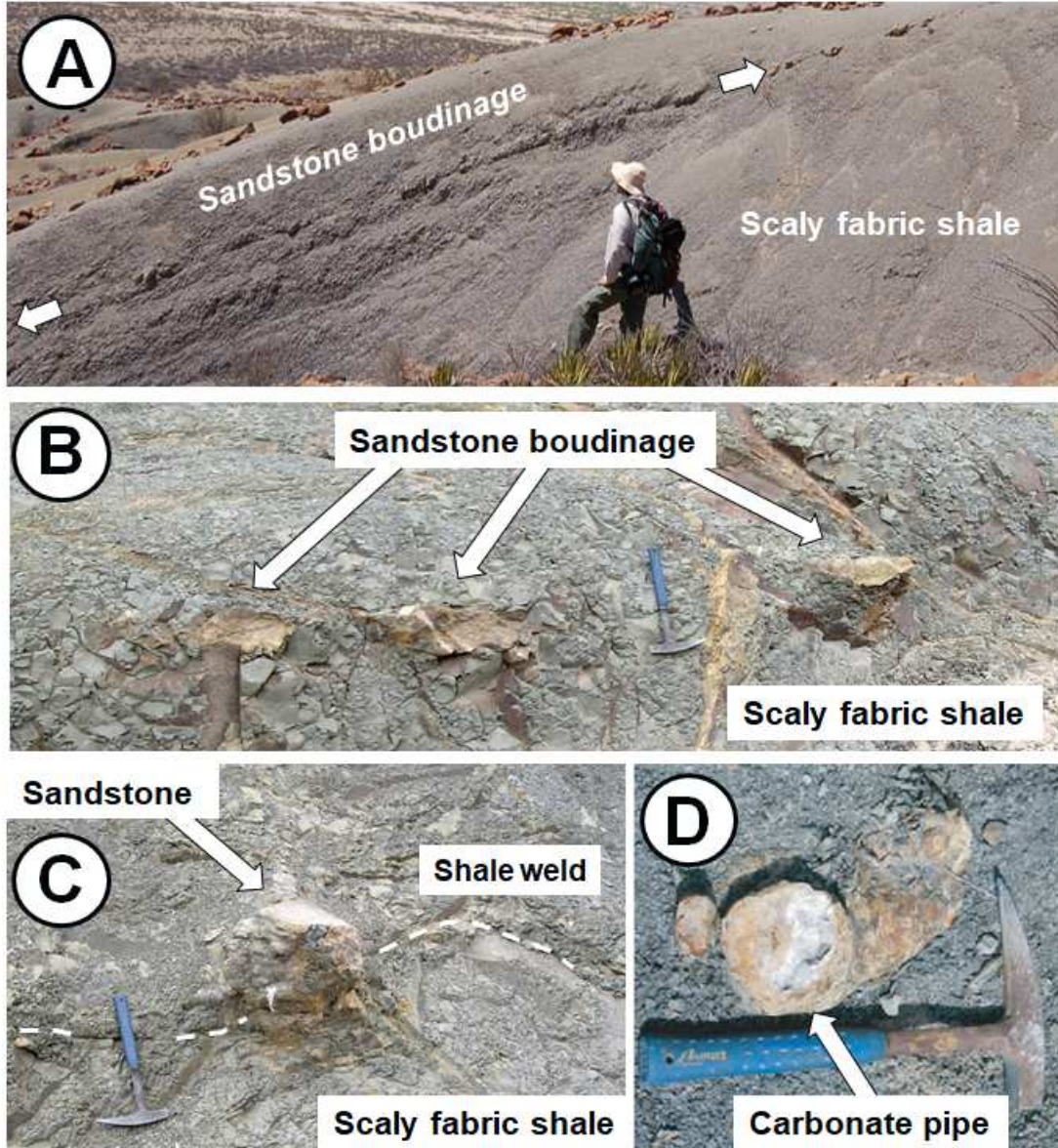
1147  
1148  
1149  
1150  
1151  
1152  
1153  
1154  
1155  
1156  
1157

**Fig. 8. A.** Continuous stratification in the Parras shale located above the Coahuila group and below the basal decollement (location of sample 132 located in Fig. 6A and cross-section 6B). **B.** The breccias observed at the top of the pelagic carbonates of the Coahuila group. These rocks correspond to anisotropic fracturing with mass precipitation of carbonate cements (large calcite crystals) precipitated in a single generation. We interpret these rocks as the result of natural hydraulic fracturing (location sample 83 located in Fig. 6A and cross-section 6B).



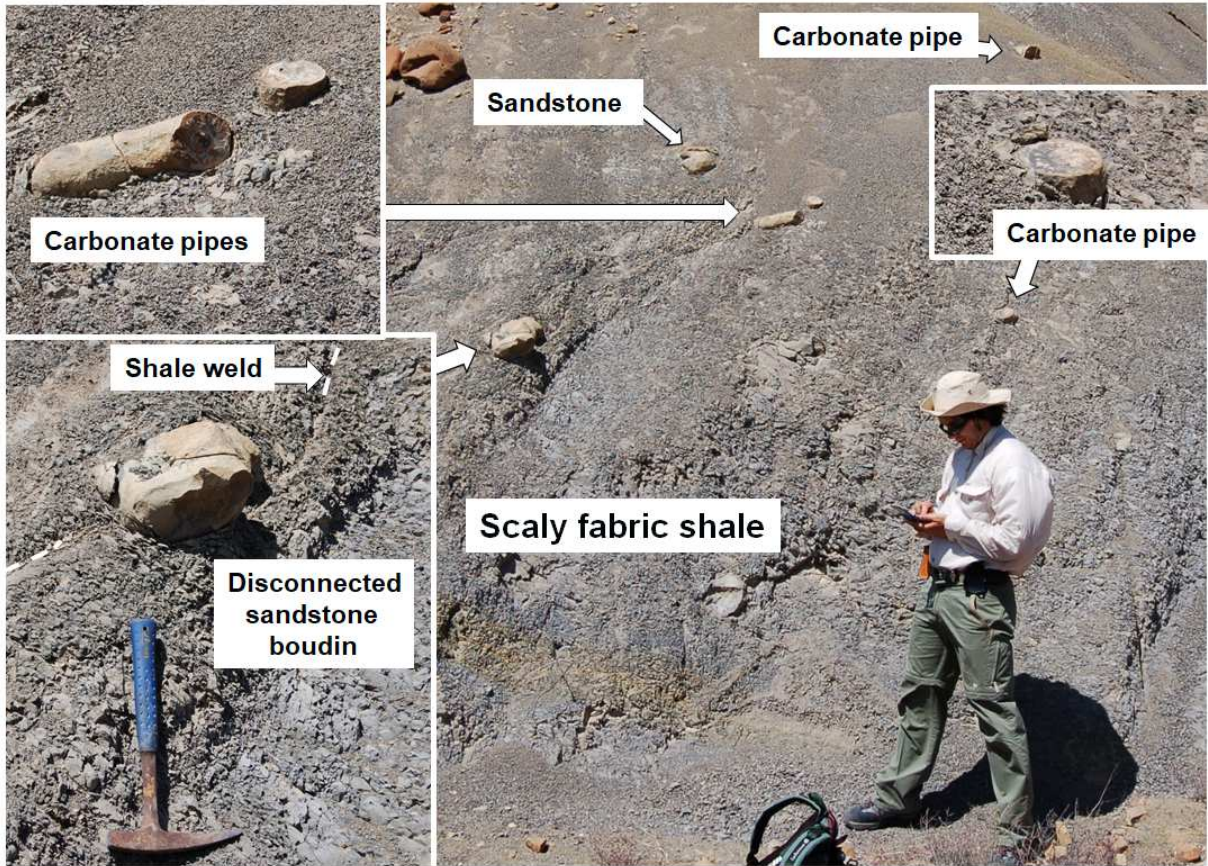
1158  
1159  
1160  
1161  
1162  
1163  
1164

**Fig. 9.** **A.** Carbonated concretions in the Parras shale formation located in the decollement area. **B.** Carbonated diffuse zones interpreted as traces of ancient fluid migration pathways within shale above the decollement. **C.** The decollement zone: Scaly fabric shale associated with massive cataclasites and tectonic breccias in the basal decollement.



1166  
1167  
1168  
1169  
1170  
1171

**Fig. 10.** “Mobile shale”: how it looks like on the field in the zone located above the decollement (Campanian Parras shale). **A.** Homogeneous scaly fabric shale with disrupted stratification and intense boudinage of sandstone layers. **B.** and **C.** Isolated boudinated element of sandstone within deformed scaly fabric shale. **D.** Carbonate tube interpreted as a fossil fluid conduit through the scaly fabric shale layers.



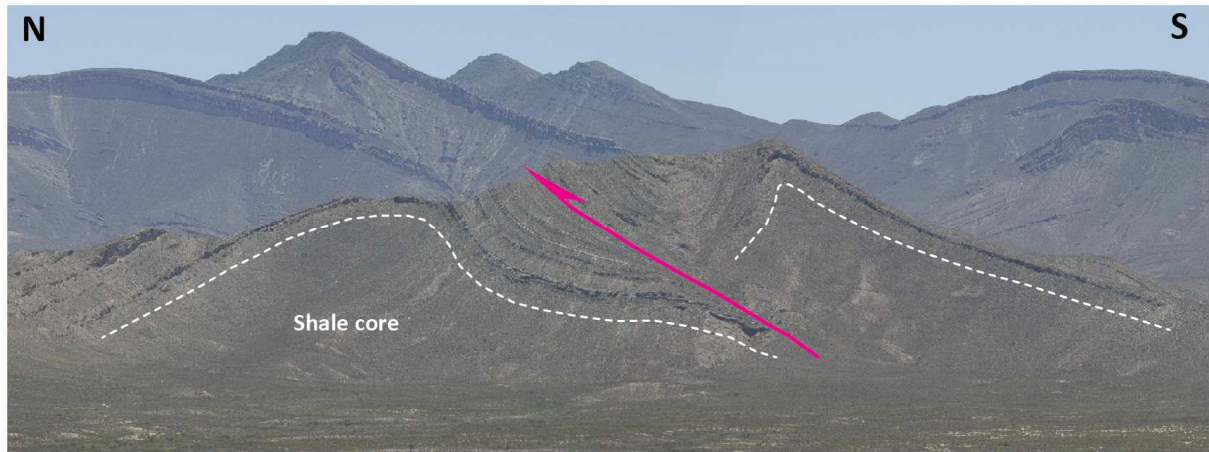
1172  
1173  
1174  
1175  
1176

**Fig. 11.** ‘Mobile’ scaly fabric shale with sandstone boudins and fluid conduits in the shale-rich cores of the main anticlines.



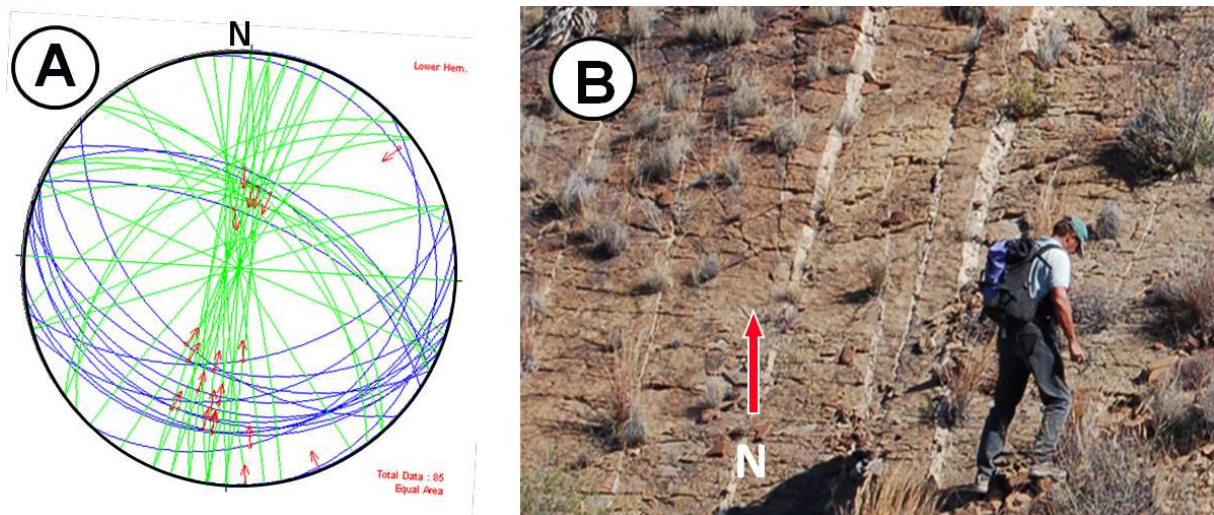
1177  
1178  
1179  
1180  
1181  
1182  
1183

**Fig. 12** - Thrust plane mineralized by carbonate cements cross-cutting the “mobile” scaly fabric shale. This structure is located in the core of a large fold (location in Fig. 7).



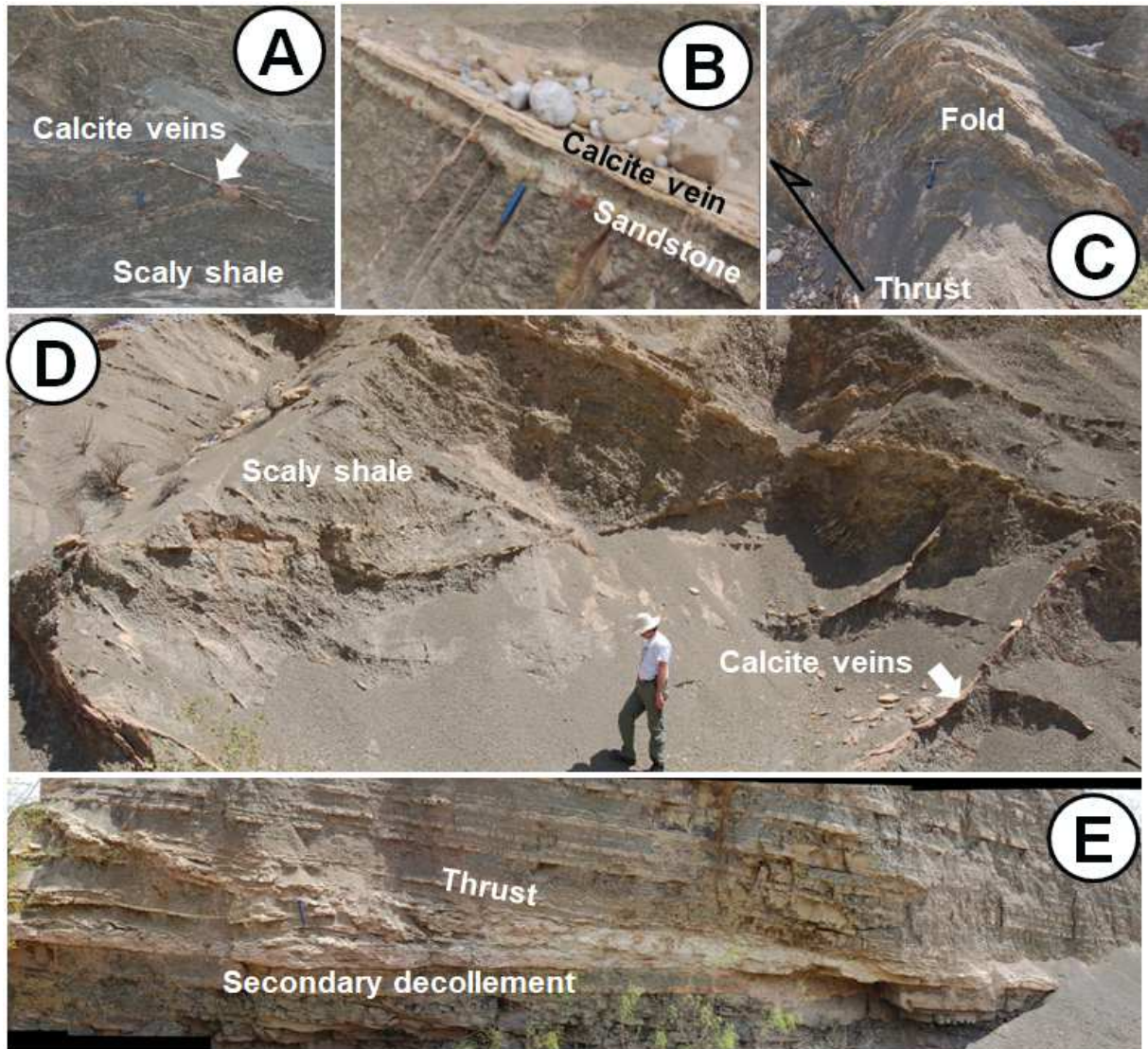
1184  
 1185  
 1186  
 1187  
 1188  
 1189  
 1190  
 1191  
 1192  
 1193

**Fig. 13** - Sandstone-rich top of the shale-rich core of large folds. Note that the top of the 'mobile shale' of the core of the folds is not intrusive within the upper layers. It is faulted as the upper layers.



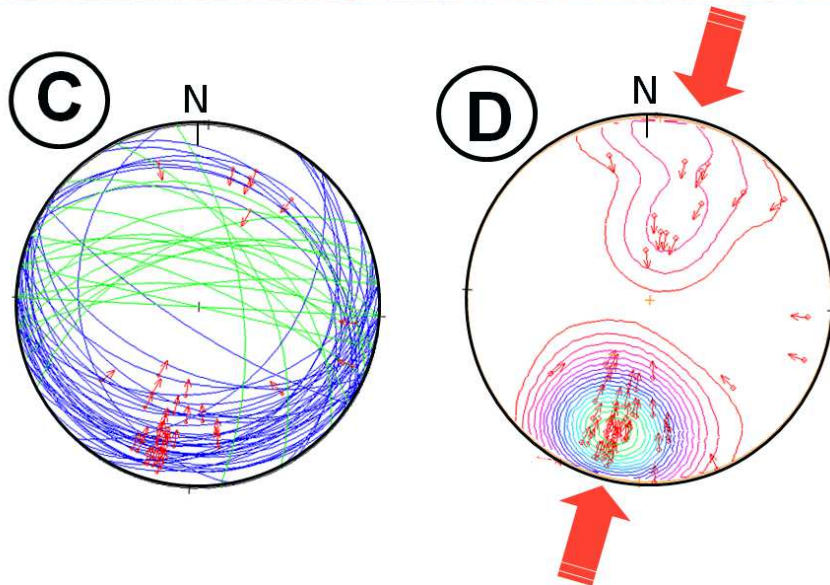
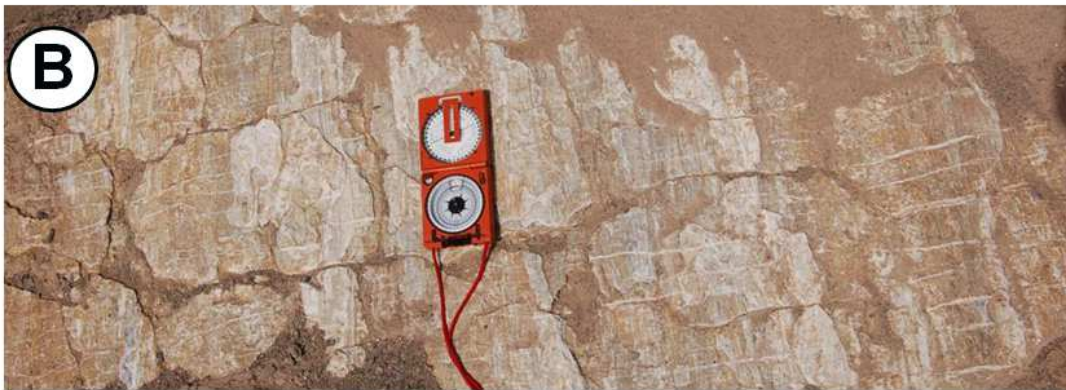
1194  
 1195  
 1196  
 1197  
 1198  
 1199  
 1200  
 1201  
 1202

**Fig. 14** - Fracturing processes of the sandstone-rich envelop of the limbs of the main folds. **A.** Stereonet of fracture measurements. Note the abundant subvertical fractures trending  $N15^\circ$  parallel to the slickenlines of the fault planes (blue: faults, red arrows: slickenlines on fault planes; green: open fractures; projection lower hemisphere equal area; 85 measurements). **B.** Cemented opened fractures trending  $N15^\circ$ .



1203  
 1204  
 1205  
 1206  
 1207  
 1208  
 1209  
 1210

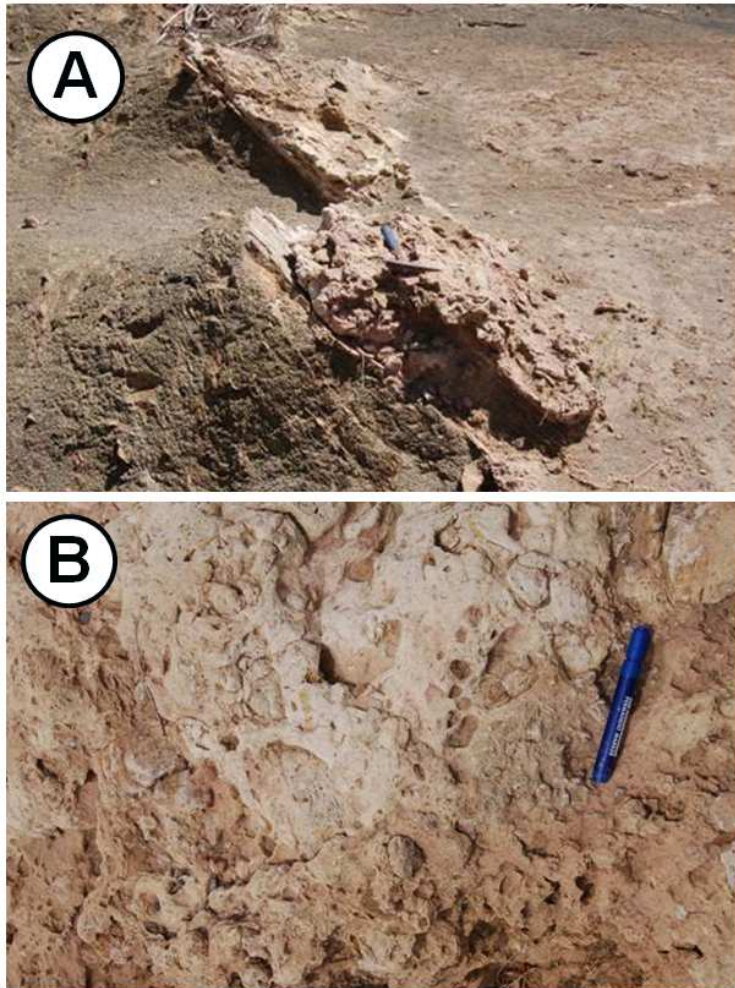
**Fig. 15.** Deformation processes in the area located above the basal decollement (Location in Fig. 7). **A.** Penetrative cleavage and cross-cutting shear bands with carbonate cements. **B.** An example of low angle fault (characterized by the precipitation of calcite) located few centimeters above a thin sandstone layer. Such features are common in the study area. **C.** A minor fold above a thrust plane. **D.** Penetrative cleavage zone with shear bands mineralized by carbonate cements. **E.** A secondary decollement with the initiation of a thrust.



1211

1212  
1213  
1214  
1215  
1216  
1217  
1218  
1219

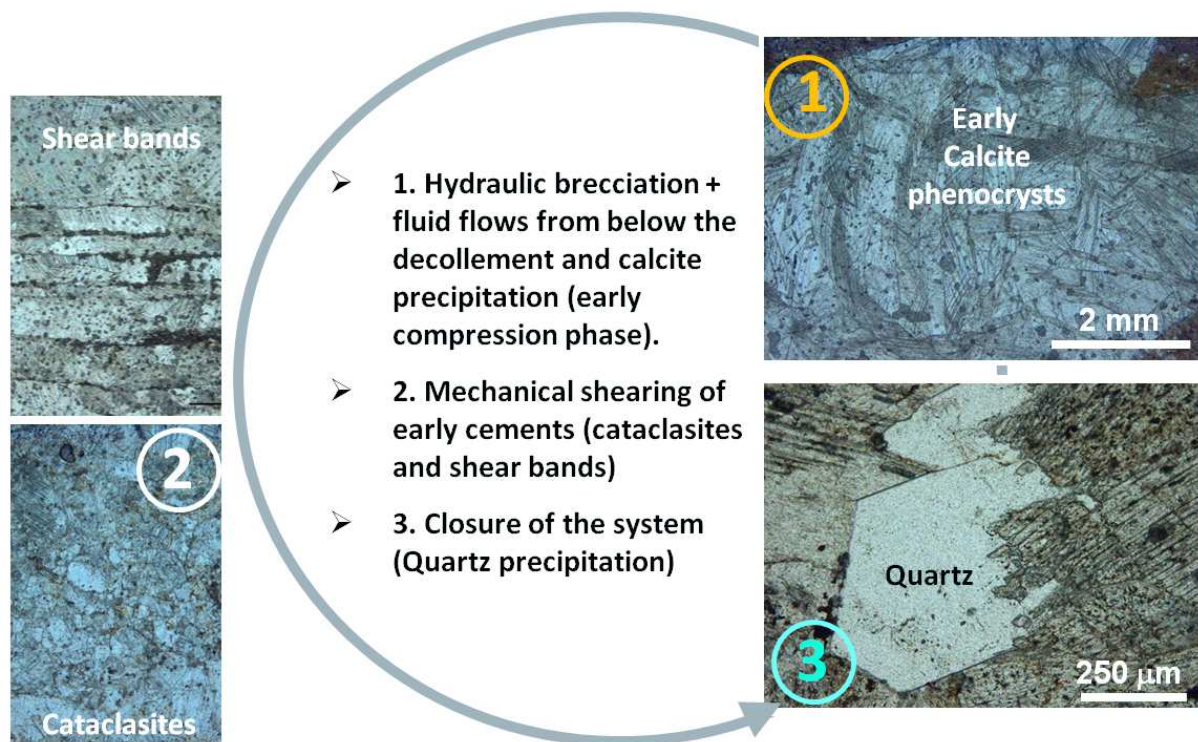
**Fig. 16.** **A.** Photo illustrating fracturing processes in and around the decollement zone. **B.** open fractures perpendicular to the slickenlines (late re-fracturing of striated calcite planes in the fault planes interpreted as the result of a late N-S extension process). **C.** Stereonet of fractures in the lower part of the thrust wedge (blue: faults, red arrows: slickenlines on fault planes; green: open fractures; projection lower hemisphere equal area; 70 measurements). **(D)** Cumulative stereonet (projection lower hemisphere equal area; 116 measurements) of slickenlines on fault planes (preferential orientation N15°).



1220  
1221  
1222  
1223

**Fig. 17.** Example of lenses of cataclasite (A) and fault breccia including polymitic clasts (B).





1225

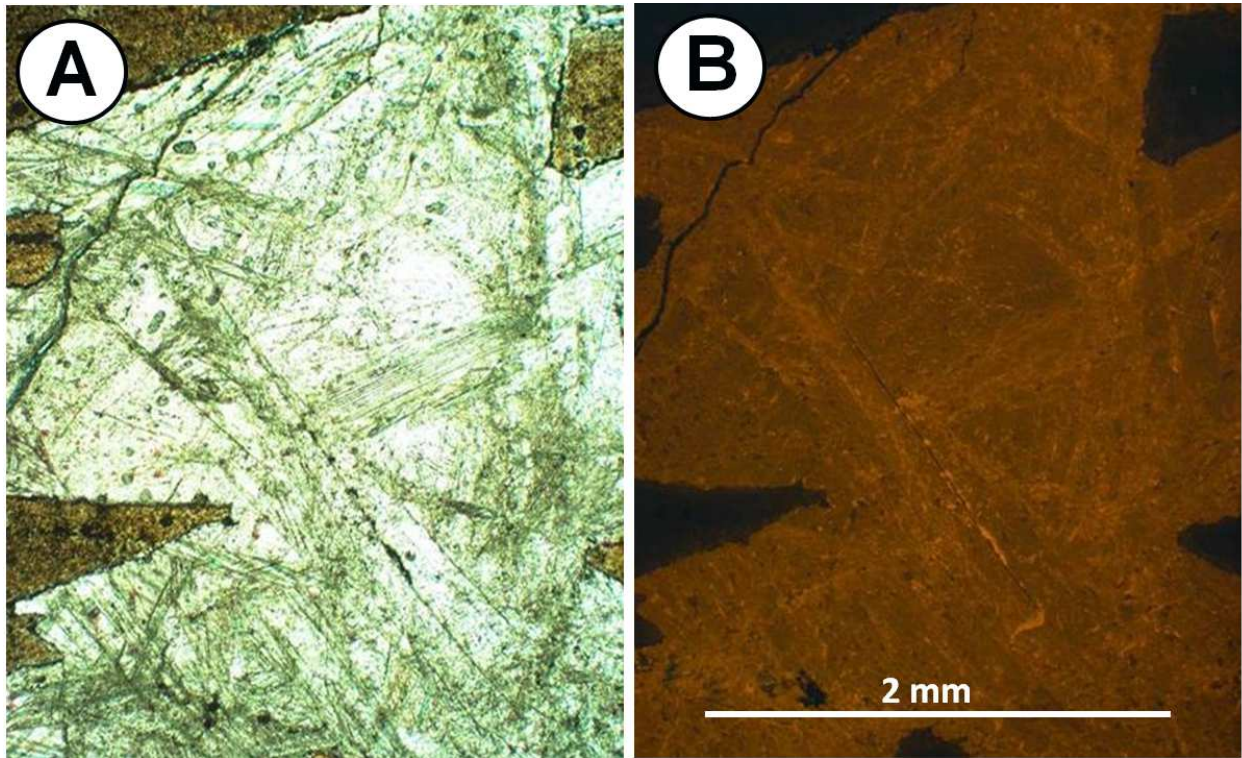
1226

1227

1228

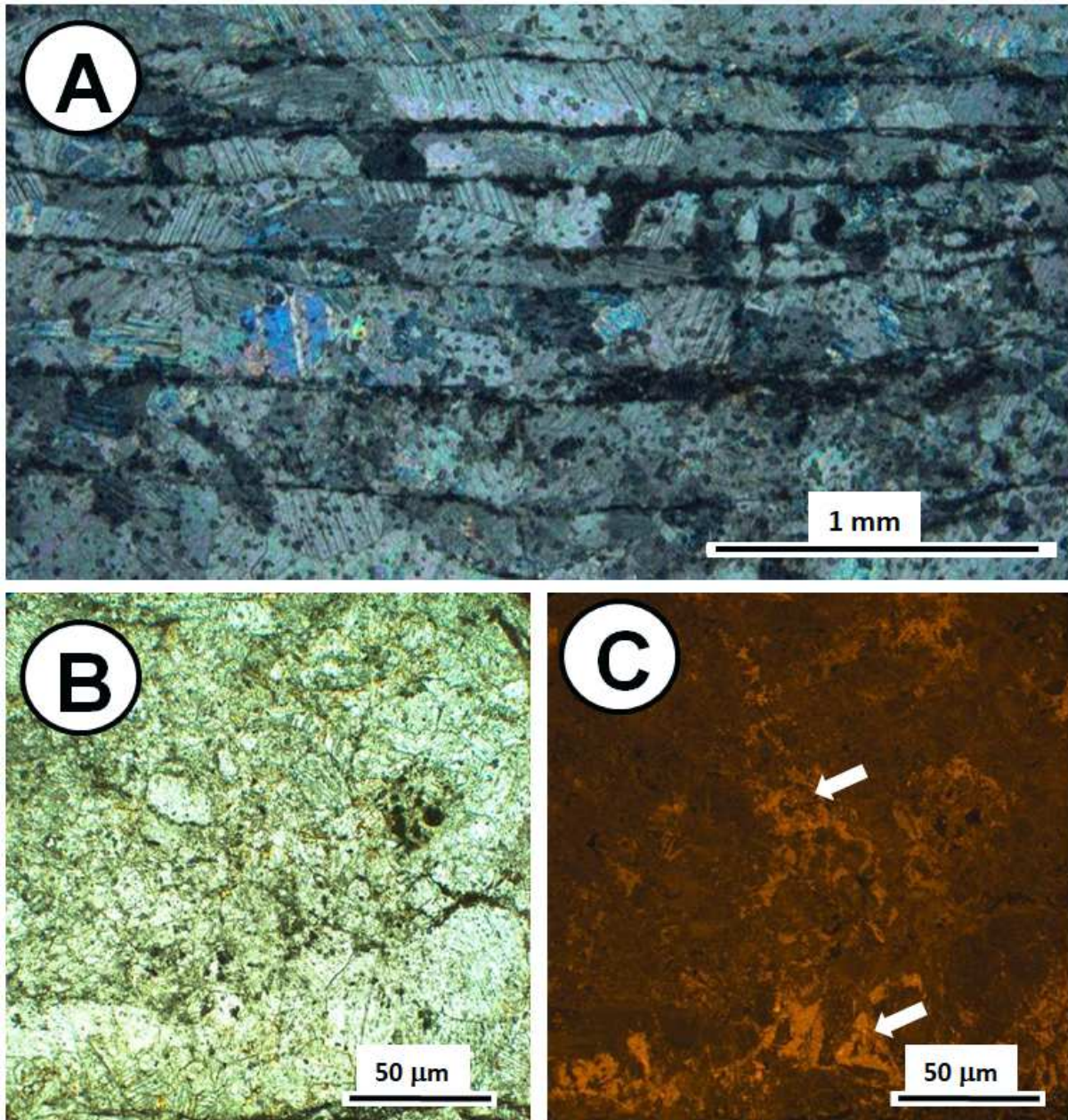
**Fig. 18.** The three main syn-kinematic diagenetic stages: 1. Calcite precipitation, 2. Cataclasites and shear bands development, 3. Quartz precipitation.

1229



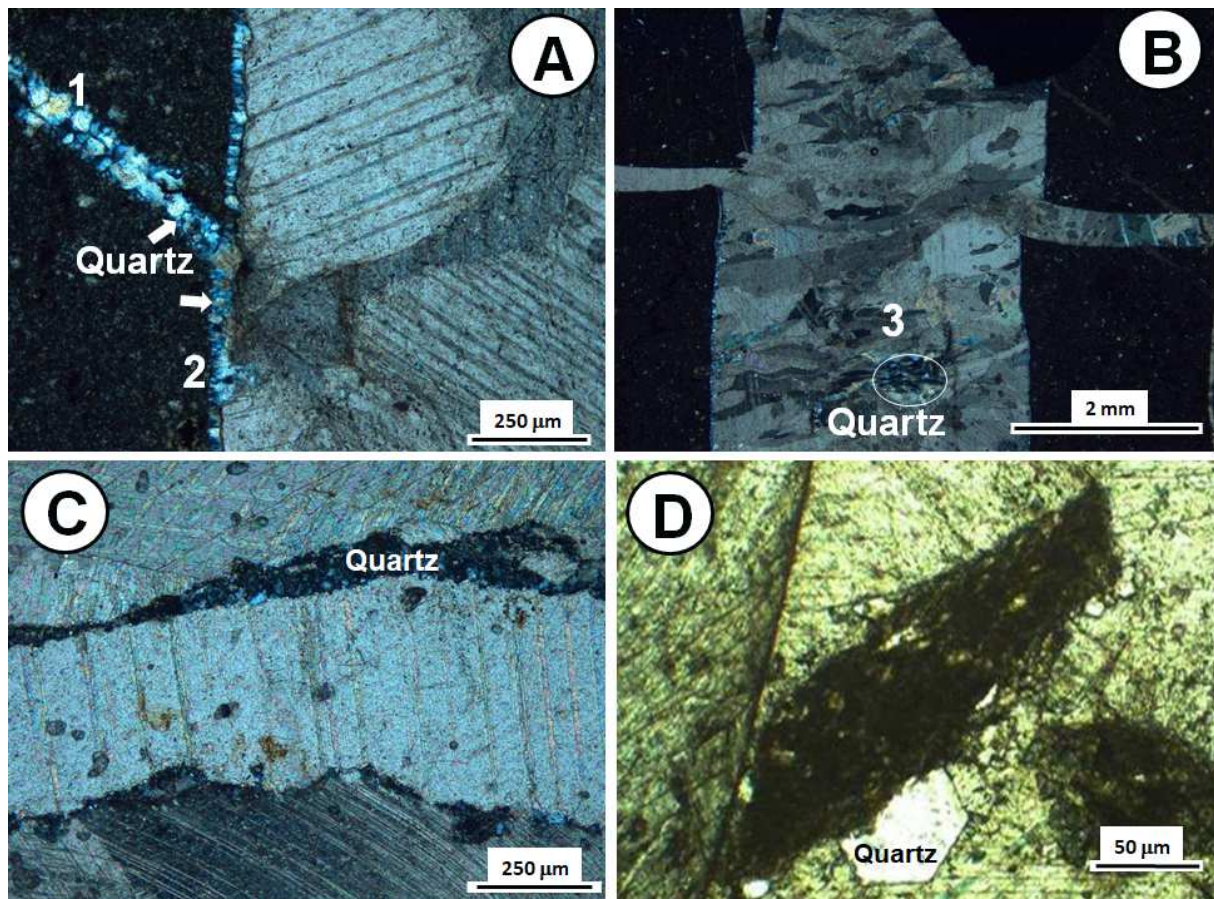
1230  
1231  
1232  
1233  
1234

**Fig. 19.** Large calcite crystals. Comparison of plane polarized light (A) and CL (B) of the calcite cement (note the homogeneous dull brown luminescence).



1236  
 1237  
 1238  
 1239  
 1240

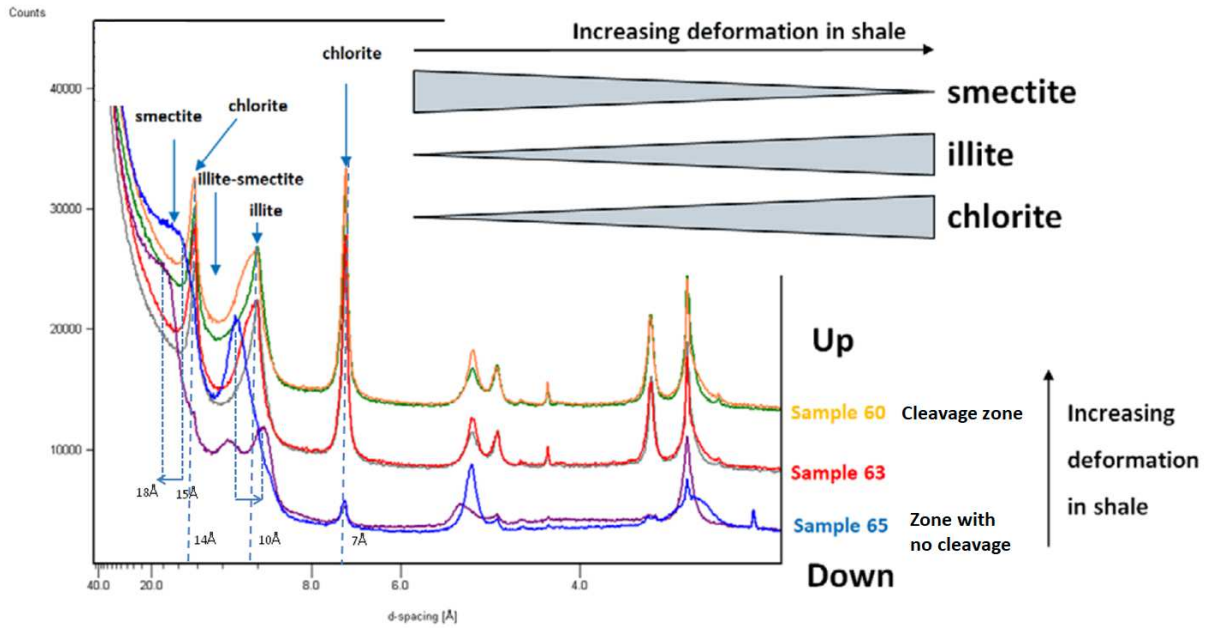
**Fig. 20.** Destruction of early cements. Sheared early calcite cements (A) and crushed early calcite cements (cataclasites) compared in transmitted light (B) and CL (C); note the presence of faint sector zoning in the less crushed calcite crystals (arrows).



1241  
 1242  
 1243  
 1244  
 1245  
 1246  
 1247  
 1248  
 1249  
 1250

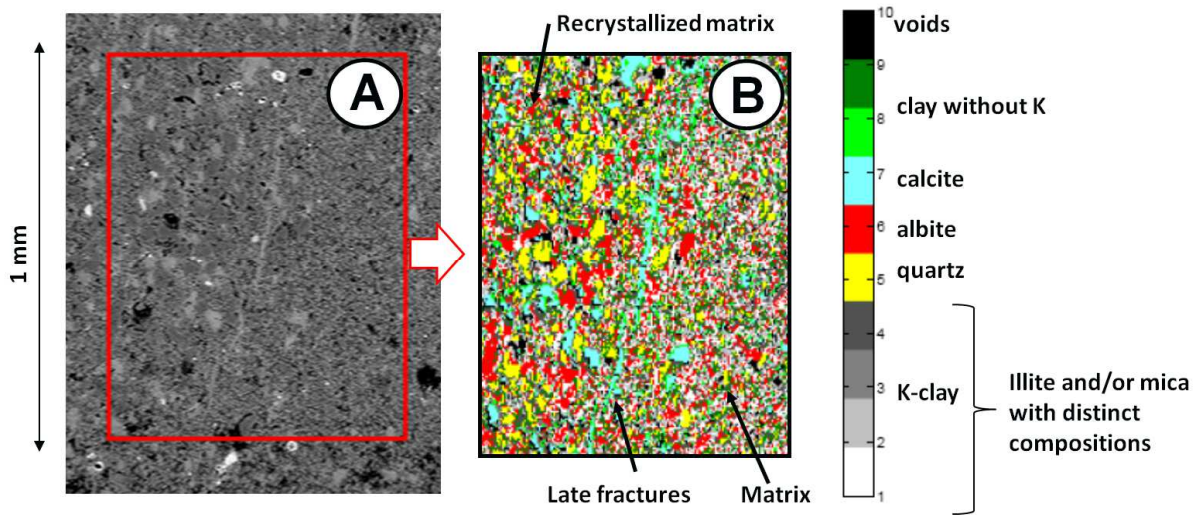
**Fig. 21.** Quartz precipitations. **A** and **B**: Two photographs of thin section (cross-polarized light) illustrating late quartz precipitation in rocks sampled below the basal decollement, either (1) as newly-formed veins, or (2) on the side of previous calcite veins (**A**), or else (3) in the core of sparitic calcite veins (**B**). **C**: Syn-kinematic late quartz veins in rocks sampled above the basal decollement (polarized light). **D**: Precipitation of quartz at the periphery of claystone clasts (host) (plane polarized light).

1251  
1252  
1253



1254  
1255  
1256  
1257  
1258  
1259  
1260  
1261

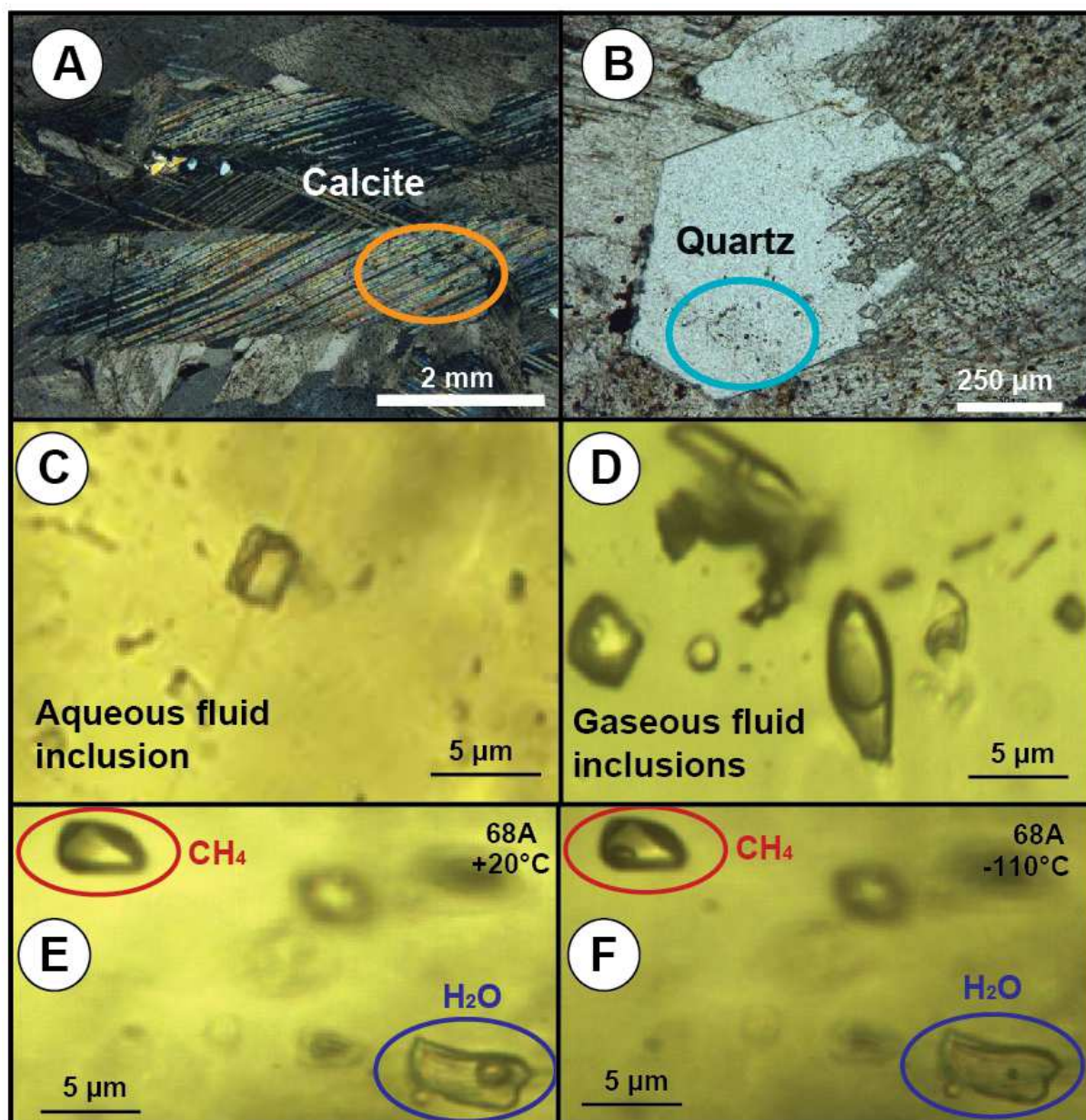
**Fig. 22.** XRD analysis results showing gradient of illitization in the cleavage zones showing the influence of the deformation on the mineralogical transformation of clays (see explanation in the text; sample location in Fig. 6A).



1262  
1263  
1264  
1265  
1266  
1267

**Fig. 23.** The structure and transformation of clay minerals in scaly shale characterized by scanning electronic microprobe (A. SEM textural view; B. SEM mineralogical mapping; sample from outcrop shown in Fig. 15D; location in Fig. 7)

1268  
1269



1270  
1271  
1272  
1273  
1274  
1275  
1276

**Fig. 24.** Characteristic fluid inclusions (sample 68A; location in Fig. 6A): Fluid inclusions in calcite (A.) and in quartz (B.), circled areas correspond to zones of high density of fluid inclusions; C. Aqueous fluid inclusions in calcite; D. Gaseous fluid inclusions in calcite. Cogenetic CH<sub>4</sub>-dominant and H<sub>2</sub>O-dominant fluid inclusions observed in calcite at 20°C (E) et -110°C (F).

1277

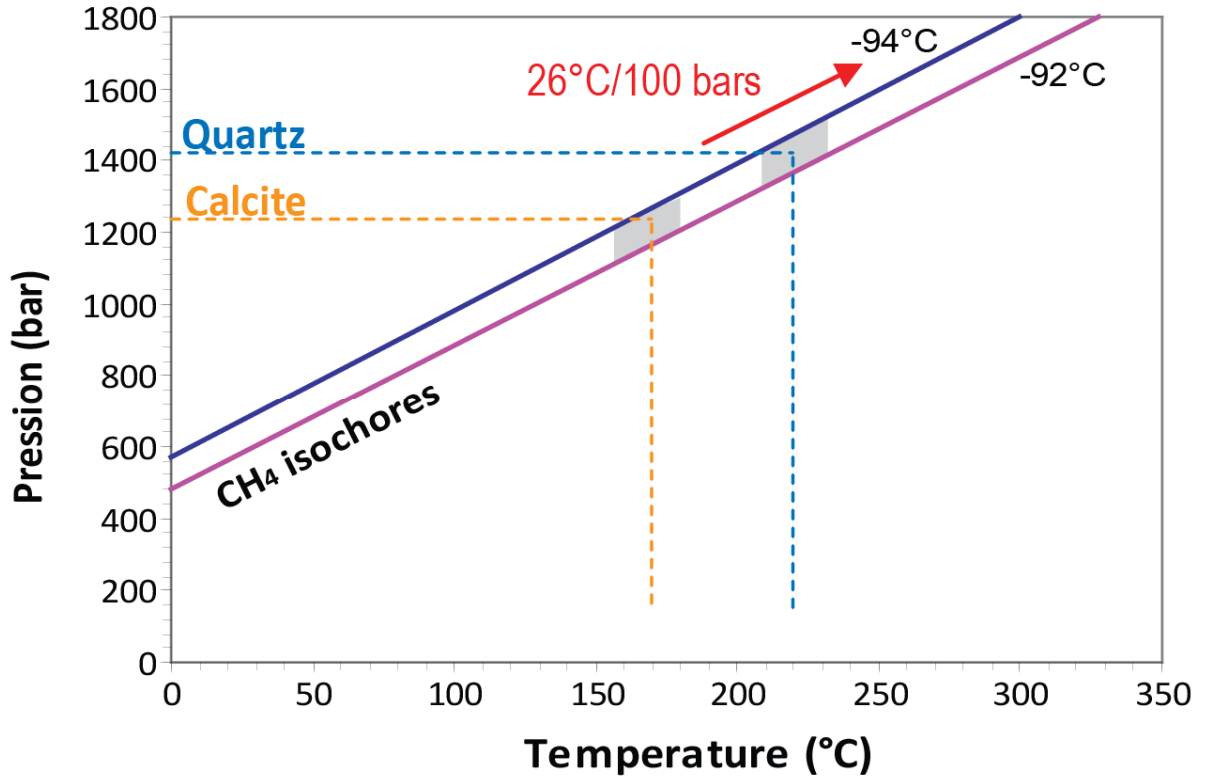
Mineral	Structural context	Sample	T <sub>fm</sub> (°C)	T <sub>mi</sub> (°C)	T <sub>h</sub> (°C)	Est. burial (km)	Correction (°C)	T trapping (°C)
Calcite	Shale-rich fold core	107B	-49	-0.5	130	5	25	155
	Top decollement zone	64A	-53	-0.5	160	5.4	-	160
	Upper decollement zone	68A	-51	-1	170	5.5	-	170
	Decollement sole thrust	132	-49	0	170	6	30	200
	Top Coahuila carbonates	83	-	-0.5	180	7	35	215
Quartz	Top decollement zone	64A	-	0	215	-	-	215
	Upper decollement zone	68A	-	0	220	-	-	220

1278

1279

1280 **Table 1.** Melting temperatures and estimated trapping temperatures of aqueous fluid  
1281 inclusions (samples location in Fig. 6A).  $T_{fm}$  : first melting temperature of ice;  $T_{mi}$  : final  
1282 melting temperature of ice;  $T_h$  : homogenization temperature; Est. burial: estimated burial as  
1283 shown in Fig. 6B; temperature corrections were made in fluid inclusions with no presence of  
1284 methane; T trapping: temperature of trapping of the fluid inclusions.

1285



1286

1287

1288

1289

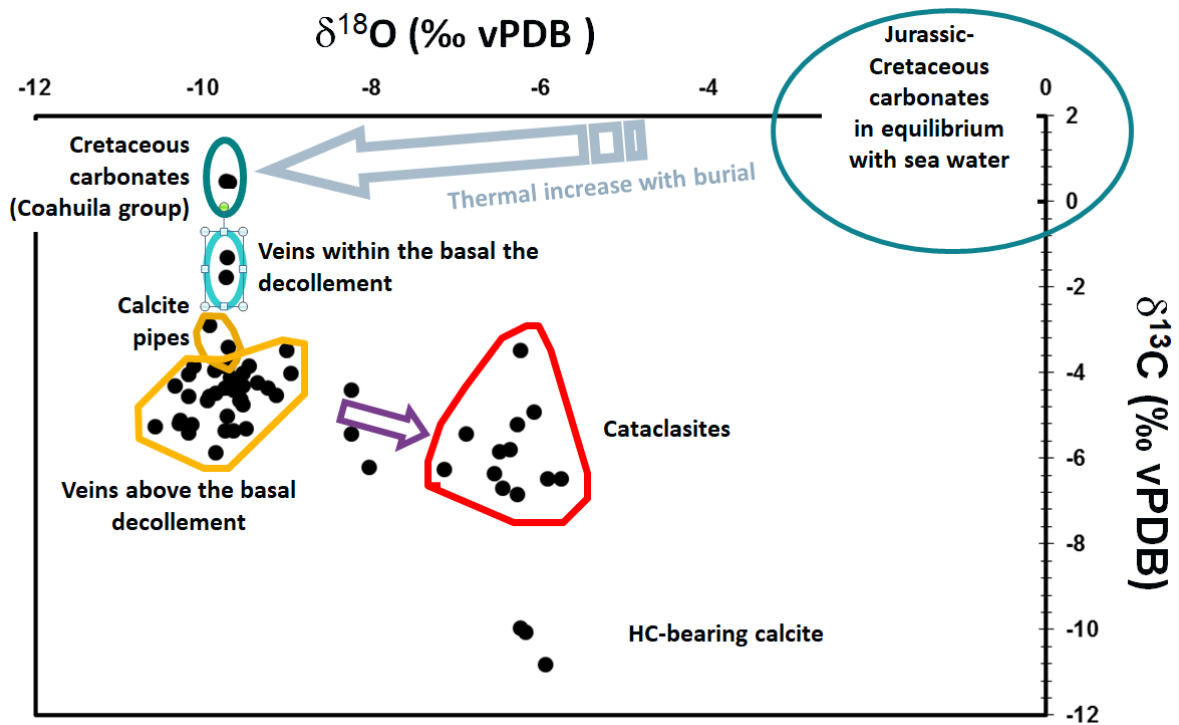
1290

1291

1292

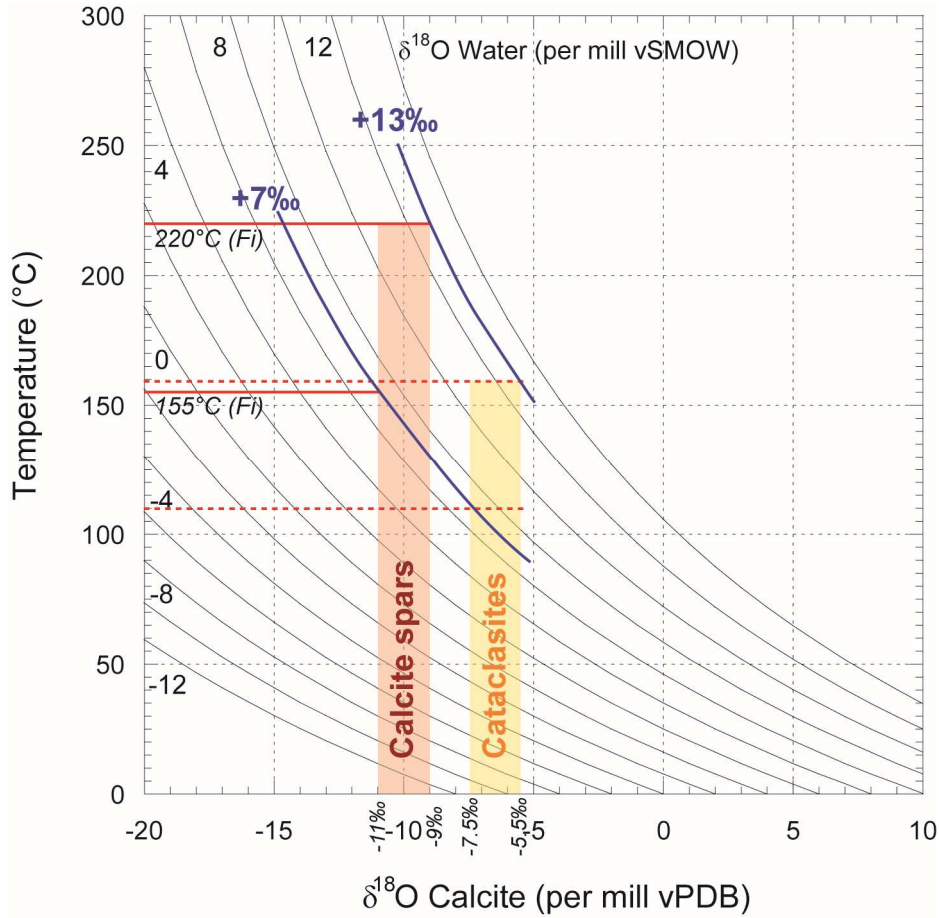
**Fig. 25.** Trapping pressure and temperature of aqueous fluid inclusions which are saturated with dissolved methane of sample 68A (location in Fig. 6A). In this case, the measured  $T_h$  are equivalent to the trapping temperatures. Methane isochores from Setzmann and Wagner (1991). Calcite:  $T=165-170^\circ\text{C}$ ;  $P= 1240\pm 40$  bars, quartz:  $T=225-230^\circ\text{C}$ ;  $P= 1430\pm 50$  bars.





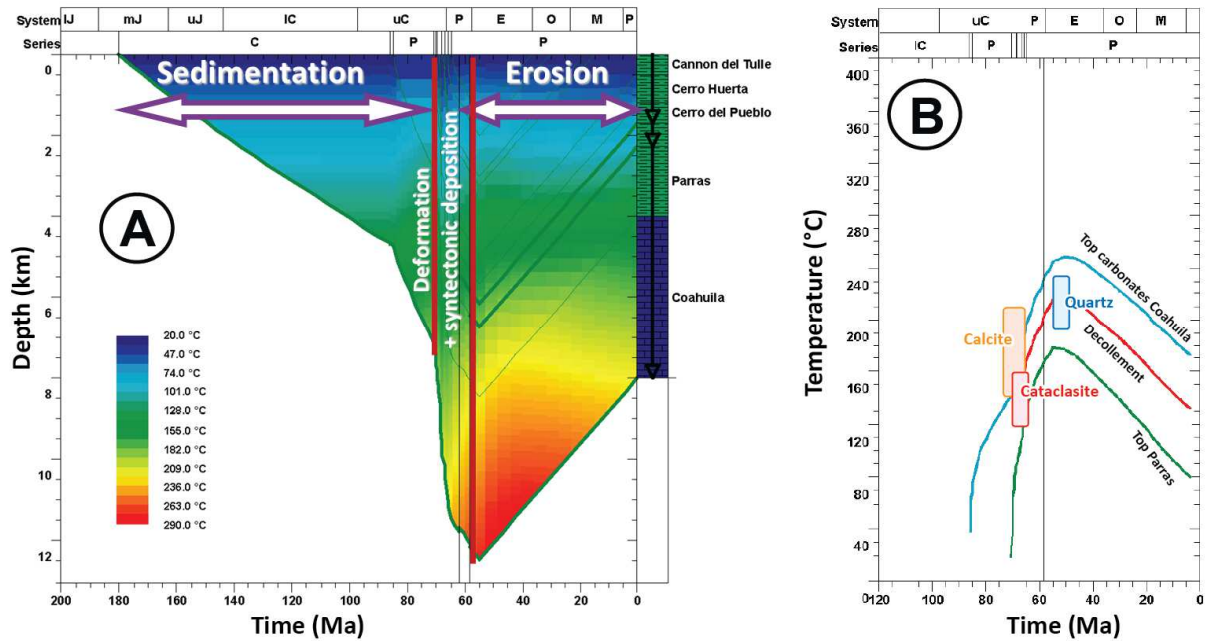
1293  
 1294 **Fig. 26.** Diagram  $\delta^{18}\text{O}/\delta^{13}\text{C}$  of calcite cements in fractures of the Parras Basin. The low  $\delta^{18}\text{O}$   
 1295 values in the carbonates of the Coahuila group are consistent with a high burial. The  
 1296 carbonates cements of the calcite tubes and veins within the Parras shale located within and  
 1297 above the decollement precipitated in similar thermal conditions. Cataclasites show higher  
 1298  $\delta^{18}\text{O}$  corresponding to lower thermal conditions. The lowest  $\delta^{13}\text{C}$  values of calcites above the  
 1299 decollement are probably related to an enrichment in light carbon during maturation of  
 1300 organic matter.

1301



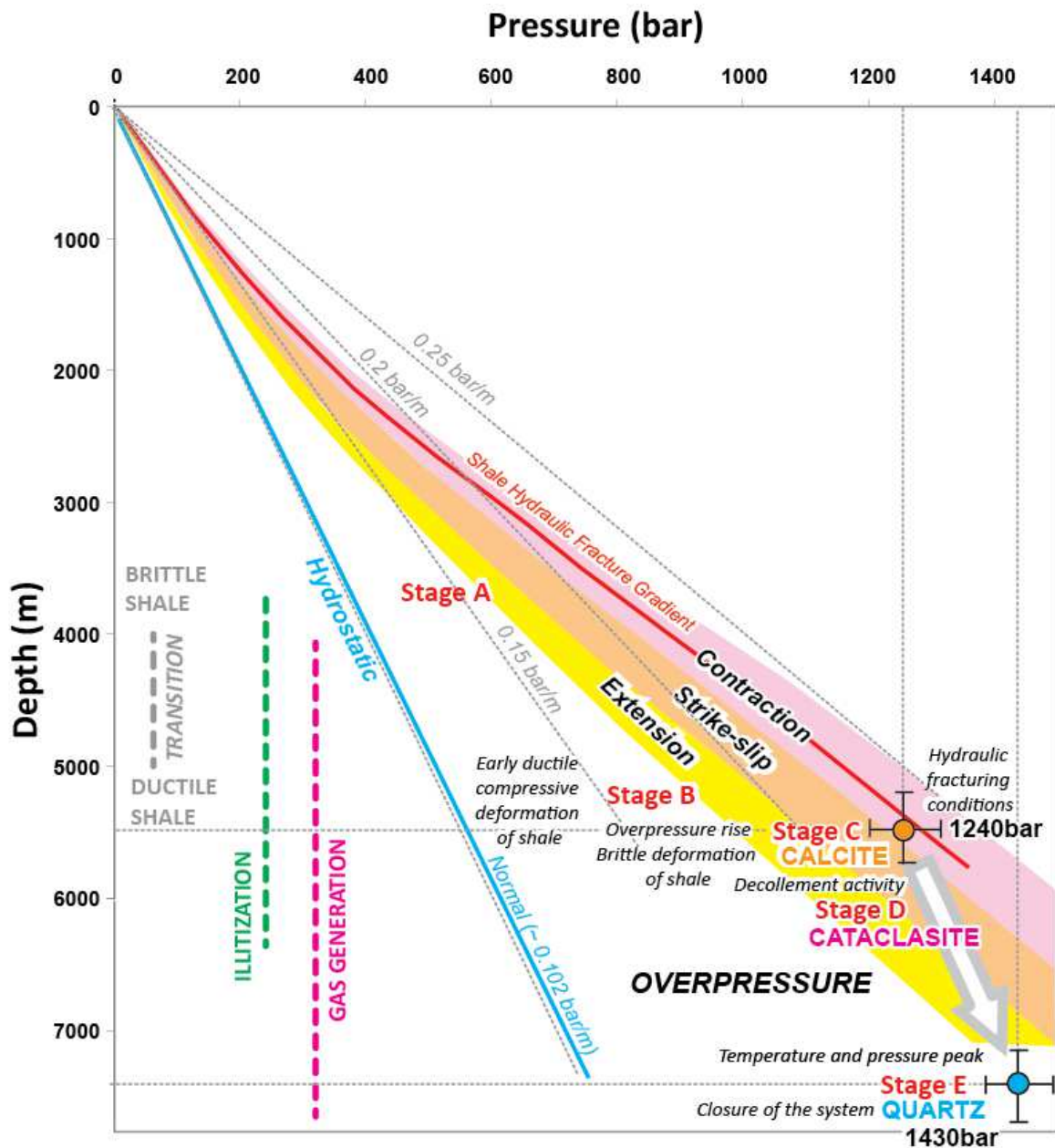
1302  
1303

1304 **Fig. 27.** Fractionation diagram for calcite in the calcite cements of the fractures of the Parras  
1305 Shale (curves constructed with the equation of O'Neil et al., 1969). Crystallization  
1306 temperatures of calcite (between 155 and 220°C) are obtained directly from the  
1307 microthermometry study of fluid inclusions. Formation of cataclasites by crushing of former  
1308 calcite spars is probably occurring at lower temperatures in the range of 110°-160° (see  
1309 discussion in the text).



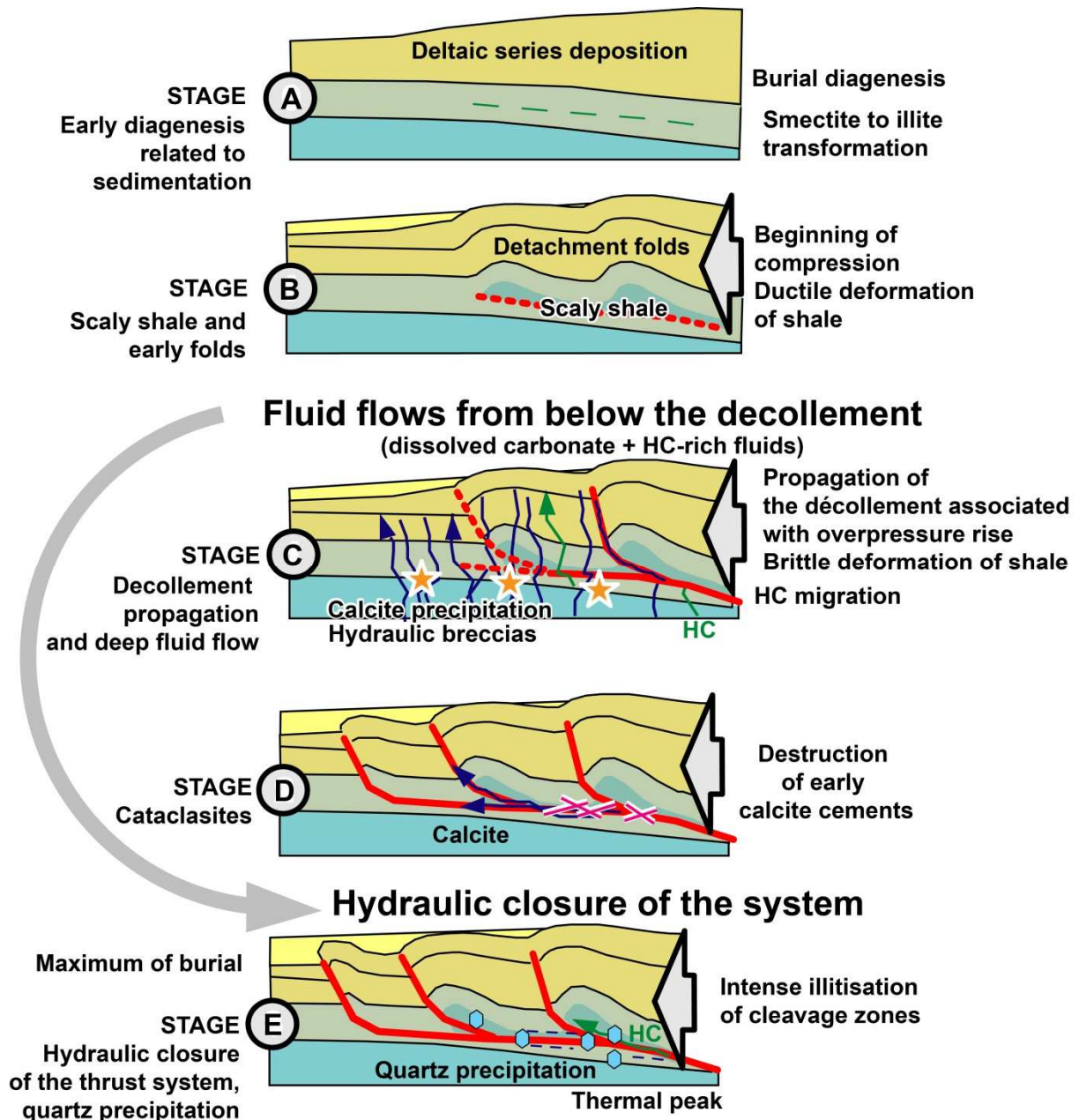
1310  
1311

1312 **Fig. 28.** A. The main stages of the modeled thermal history (IJ: Early Jurassic, mJ: Mid-  
1313 Jurassic, uJ: Late Jurassic, IC: Early Cretaceous, uC: Late Cretaceous, P: Paleocene, E:  
1314 Eocene, O: Oligocene, M: Miocene, P: Plio-Quaternary). A progressive increase of the  
1315 temperature occurred during sedimentation, then an acceleration of the increase of  
1316 temperature occurred in relation with higher sedimentation rates before contraction tectonics  
1317 coupled with a syn-tectonic sedimentation, finally, a phase of cooling occurred linked to the  
1318 erosion of the system. **B.** Syn-kinematic diagenetic events replaced within the thermal history.  
1319 1. Calcite precipitation associated with hydraulic fracturing and rapid percolation of hot fluids  
1320 of deep origin (not in equilibrium with the host rocks in the decollement area but in  
1321 equilibrium with the rocks Coahuila carbonates; hydrothermal type); 2. Cataclasites  
1322 recrystallization at the thermal conditions of the host rocks in the decollement area (lower  
1323 thermal conditions compared to calcite); 3. Quartz precipitation at the thermal peak.



1324  
 1325  
 1326  
 1327  
 1328  
 1329  
 1330  
 1331  
 1332

**Fig. 29.** Estimate of pressure-depth conditions for the sample 68A deduced from the study of fluid inclusions. On this graph, we also attempt to replace the different stages of deformation and diagenesis described in the text. The hydraulic fracturing conditions *versus* the structural context are estimated from a compilation of global values of minimum leak-off pressure from Grauls (1998) and Deville et al. (2010). The present case study corresponds to contraction conditions (minimum stress vertical).



1333  
1334  
1335

**Fig. 30.** Schematic model of deformation - fluid migration – diagenesis relationships.